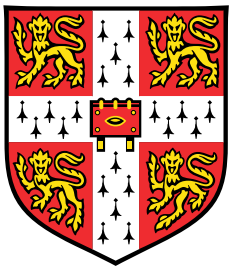

Nonlinear hydrodynamic instability and turbulence in eccentric astrophysical discs

Aaron Wienkers

Supervisor: Prof. Gordon Ogilvie

Department of Physics
University of Cambridge

This dissertation is submitted for the degree of
Master of Philosophy

Trinity College September 2016

To my parents,
Kevin and Cindy Wienkers,
And all of my friends,
Without whom none of my success would be possible.

Declaration

I hereby declare that except where specific reference is made to the work of others, the contents of this dissertation are original and have not been submitted in whole or in part for consideration for any other degree or qualification in this, or any other university. This dissertation is my own work and contains nothing which is the outcome of work done in collaboration with others, except as specified in the text and Acknowledgements. This dissertation contains fewer than 15,000 words including appendices, bibliography, footnotes, tables, and equations.

Aaron Wienkers
September 2016

Acknowledgements

I am indebted to my supervisor, Prof. Gordon Ogilvie, for his patient guidance and invaluable insight which has made this research both possible and truly enjoyable. Thanks are also due to the members of the Centre for Scientific Computing for many helpful discussions.

I must also gratefully acknowledge the support of the NSF Graduate Research Fellowship and the Extreme Science and Engineering Discovery Environment (XSEDE) for granting me the necessary computing resources to undertake this endeavour.

Abstract

The nonlinear evolution of the parametric instability of inertial waves inherent to eccentric discs is studied by way of a new local numerical model. Mode coupling of tidal deformation with the disc eccentricity is known to produce exponentially growing eccentricities at mean-motion resonances, most prominently via the 3:1 eccentric Lindblad resonance in circumstellar binaries. However, the details of an efficient saturation mechanism for this growth are still not fully understood. Linear theory for the parametric instability of inertial waves in eccentric discs has previously been studied by Barker and Ogilvie (2014), the nonlinear evolution of which dictates the transport rates and may help saturate this unmitigated eccentricity growth. This thesis develops a generalised numerical model for an eccentric quasi-axisymmetric shearing box based on the theoretical model developed by Ogilvie and Barker (2014) which itself generalises the often-used local cartesian shearing box model. The numerical method is an overall 2^{nd} order well-balanced finite volume method which maintains the stratified and oscillatory steady state solution to machine precision.

This implementation is employed to study the nonlinear outcome of this parametric instability in eccentric discs with vertical structure. Stratification is found to constrain the perturbation energy near the midplane, and localises the effective region of the secondary instability. A saturated marginally sonic turbulent state is then maintained by the breaking of inertial waves cascading energy into smaller scales. The resulting turbulence is quite inefficient at transporting angular momentum through the disc, as might be expected from a restricted axisymmetric instability. Still, the saturation of this parametric instability of inertial waves is shown to damp the eccentricity on the timescale of 50 to 100 orbital periods, and so is a promising mechanism for balancing the exponential growth of eccentricity from the eccentric Lindblad resonances.

Table of contents

List of figures

Chapter 1

Introduction

Astrophysical discs are a common phenomenon in the universe — from galaxies and their resident active galactic nuclei, to x-ray binary stars, protoplanetary discs, and planetary rings. These discs are all characterised by rotationally-supported matter in a stable orbit around a central gravitating object. Accretion discs are an interesting subset of these discs because they support a radial inflow of mass and thus mass accretion onto a central object. Accretion discs form when an external source of in-falling matter has excess angular momentum and thus settles into a flattened disc (if the medium is collisional, i.e., gaseous). Since these discs are often dominated by centripetal support against gravity, they are differentially rotating which appears locally as a background shear flow. This shear flow contains a vast source of energy, which in non-rotating systems (such as plane Couette flow) would be fluid-dynamically unstable at these high Reynolds numbers. It may then be surprising at first glance that these shearing discs don't immediately become unstable, dissipate orbital energy, and infall onto the central object. Indeed this does not happen because the system is additionally restricted by angular momentum conservation. Thus in a rotating system, energy liberation must be accompanied with the transport of angular momentum radially outwards while mass accretes inwards. All accretion discs consequently require a mode of angular momentum transport out of the disc to continue supporting mass accretion.

Unfortunately, molecular viscosity alone cannot account for the observed transport rates of mass and angular momentum through the disc. Acting solely on the background shear, molecular viscosity can produce effective α-viscosity values of only 10^{-10} to 10^{-8} (Shakura and Sunyaev, 1973), often implying that the molecular viscous timescale is very much longer than the lifetime of the disc itself! Thus to explain observations, an α-viscosity near 10^{-3} to 10^{-1} is required (Spitzer, 1962). For many years, attention

has been focused on searching for efficient modes of transporting angular momentum that might explain this deduced rate of mass accretion through observable discs. An enhanced, turbulent viscosity can often significantly exceed that of molecular viscosity, though the origin of the required turbulence is still elusive in particular scenarios and quite debated. The magneto-rotational instability is now being accepted as the most promising means of driving turbulence to enhance this viscosity (Balbus and Hawley, 1991); however, it is only effective in ionised regions of the disc.

Razor thin viscous circular accretion discs in particular have been the subject of early seminal theories (Pringle, 1981). Yet there are no widely accepted local purely hydrodynamic instabilities in cylindrical discs efficient enough to explain the deduced rate of mass accretion through observable discs. Thus by lifting the assumption of a cylindrical disc, additional instability and transport processes may be excited. Indeed, although the lowest orbital energy state is circular, Syer and Clarke (1992) have shown that not every disc tends to circularise. Lin and Pringle (1976) have shown circularisation is inevitable for the special case of discs in a binary potential; however, in general this is dependent on the phase of the stresses in relation to the orbital phase. Analogous to the classic axisymmetric orbital diffusion problem for a circular ring, Syer and Clarke evolved an elliptical ring of matter, finding that the initial eccentricity can be sustained even on viscous timescales for aligned orbits of similar eccentricities. Further mechanisms have more recently been found to couple with the evolution of eccentric disc modes and continually perturb or sustain eccentric orbits. These eccentric perturbations may be related to the origination of the disc, due to the continuous anisotropic mass transfer from a binary companion (Roche overflow) or from the parent nebular cloud core. Eccentricity may also be sustained by a viscous instability to eccentric perturbations which is known to exist for particular viscosity prescriptions, including the often-used α-viscosity (Lyubarskij et al., 1994). On longer time-scales, secular interactions with an eccentric companion or planet are also known to induce eccentricity. Finally, eccentric mode-coupling with a tidal deformation via a mean-motion resonance has been shown to produce exponentially growing eccentricities when the disc and perturbing companion orbital frequency are nearly in a ratio of m to $m \pm 2$ (Lubow, 1991, 2010). These mean-motion resonances may arise in planetary rings resonating with satellites (Goldreich and Tremaine, 1981), protostellar discs with embedded planets (Kley and Dirksen, 2006; Papaloizou et al., 2001), as well as circumstellar or circumbinary discs perturbed by the stellar binary (Lubow, 1991; Whitehurst, 1988).

Thus the classical theory of accretion discs (Pringle, 1981) has been generalised to accommodate this additional degree of freedom in the orbital energy (Ogilvie, 2001). Eccentric discs store additional energy in the $m = 1$ azimuthal inertial mode, which opens up possibilities for instability and energy extraction not available to cylindrical discs. One such instability arises from the parametric coupling between small-scale inertial waves and the periodically modulated parameters of the eccentric azimuthal mode, generating growing inertial waves capable of transporting mass and angular momentum (Barker and Ogilvie, 2014; Papaloizou, 2005b). This instability may provide the necessary means of saturating the eccentricity growth, in particular from the strong 3:1 eccentric inner Lindblad resonance viable in cataclysmic binaries, and which are shown to produce unmitigated eccentricity growth in linear theory (Lubow, 1991). The details of this saturation mechanism may help explain the occurrence of outbursts and superhumps common to these binary systems, as well as the observed eccentricities of embedded planets (Goldreich and Sari, 2003). There is also interest in finding a dependence of the α-viscosity on disc eccentricity, which would contribute to higher-level analytic models allowing theorists to probe the early formation of protostellar discs, setting the initial conditions for star and planet formation.

These disc phenomena are able to be explored in a number of ways; however, upon exhausting linear perturbation theory, numerical models become an irreplaceable tool for studying the nonlinear dynamics of these accretion flows. Current numerical methods for studying eccentric discs are limited to global (entire disc) simulations. Global smoothed particle hydrodynamics (SPH) simulations (Murray, 1996; Whitehurst, 1988) were originally employed to deduce the global disc properties and eccentric instability modes; however, global finite volume and difference methods are now common (Kley and Dirksen, 2006; Kley et al., 2008; Marzari et al., 2009). Yet this parametric inertial wave instability has only ever been previously observed by Papaloizou (2005a) using a global disc model with no vertical gravity. This is likely because the majority of global simulations of eccentric discs are either 2D, and therefore unable to support this instability, or 3D but too short in duration and numerically dissipative (Bitsch et al., 2013) due to limits of computational resources. Alternatively, simulating only a subset of the disc permits using higher spatial resolutions, as well as allowing more control over the numerical studies. Thus local models have seen many advances in theories of accretion discs where global simulations fall short. However, until now no generalisation of the shearing box has been implemented to model eccentric discs.

The following work aims to establish a numerical method for the local description of eccentric discs, based on the model developed by Ogilvie and Barker (2014). This

local numerical model will subsequently be used to probe the nonlinear evolution of the parametric inertial wave instability described by Barker and Ogilvie (2014), extending the work of Papaloizou (2005b) to include vertical gravity which has been shown to be important for the dynamics of the instability. This thesis will begin with a review of the dynamics and relevant instabilities inherent to eccentric discs in Chapter 2, including how they can be probed in a controlled manner using local models to deduce global disc transport properties and subsequent evolution of the eccentricity. The finite volume methods (FVM) and local numerical model for eccentric discs are developed in Chapter 3, in addition to a number of modifications and assumptions when adapting this theoretical model. Finally, a detailed look at the nonlinear effects and breaking of inertial waves is presented in §4.1, as well as how it contributes to the saturation of the parametric instability in §4.2. A scaling of the turbulent energy dissipation with eccentricity is additionally proposed, extending the linear analysis of Barker and Ogilvie (2014). In §4.3, the turbulent transport of angular momentum is deduced, and the effect of this turbulent state on the eccentricity decay is further investigated in §4.4, where the implications for a steady disc eccentricity are discussed.

Chapter 2

Eccentric accretion discs

2.1 Background

2.1.1 Accretion disc dynamics

A global hydrodynamical model of an accretion disc may be realised by simply adding a gravitation term, $\nabla\Phi_g$, to the Euler momentum equation, where the non-self-gravitational potential at radius r, and height off the midplane, z, is $\Phi_g = -GM/\sqrt{r^2+z^2}$. This assumption that self-gravitation between fluid elements is negligible is valid for low-mass discs and quantified by the Toomre Q stability criterion (Toomre, 1964) for a Keplerian disc

$$Q = \frac{c_s \Omega}{\pi G \Sigma} > 1. \tag{2.1}$$

Here Σ is the local surface density of the thin disc, Ω is the angular velocity (orbital frequency), and $c_s = \sqrt{\gamma p/\rho}$ is the adiabatic sound speed. The addition of this radial gravitation term motivates a number of length and time scalings pertinent to astrophysical discs. Apart from the disc radius, R, a second length scale is motivated from a hydrostatic balance with the vertical component of gravity. This isothermal scale height is

$$H = \frac{c_s}{\Omega}. \tag{2.2}$$

Relating these two length scales gives a non-dimensional disc aspect ratio, H/R. Three additional pertinent timescales also come out of the Navier-Stokes equations with a central gravitational potential: the dynamical, viscous, and thermal times. The relative magnitude of each will motivate and validate a number of important assumptions. The dynamical time, $t_d \sim \Omega^{-1}$, is the timescale on which important

dynamic processes occur on, such as instability and turbulent transition. A viscous timescale, $t_v \sim R^2/\nu \sim \alpha^{-1} (R/H)^2 t_d$, sets the time for a fluid parcel to move radially through the disc solely due to momentum diffusion or transport. Here, $\alpha < 1$ is the α-viscosity parameter of Shakura and Sunyaev (1973) which gives a dimensionless measure of the rate of angular momentum transport within the disc. Finally, the thermal timescale is locally set by the ratio of the thermal heat content to the viscous heating rate and is $t_t \sim \alpha^{-1} t_d$. Thus for thin ($H/R \ll 1$) discs, $t_d < t_t \ll t_v$. It is argued based on the relative time-scales of this system that any long-term evolution can be ignored because the dynamical processes of interest are relatively quite fast. This means the evolution of the central mass may be ignored as well as viscous heating processes that could perturb the system from an initial equilibrium state. Viscosity may then be ignored altogether, and focus turned to the Euler system.

It should be acknowledged that some additional physics will not be considered here for the sake of simplicity, but which are known to be important in particular disc dynamics (Papaloizou and Lin, 1995, and references therein). Irradiation heating from the central object and radiative cooling dictate the viability of certain instabilities, in particular gravitational instability. Viscous heating also wages in this thermodynamic balance in regions of intense shear near the central object, warranting a general viscosity prescription. Most importantly in ionised discs, magnetic fields are necessary for realising the magneto-rotational instability known to locally destabilise even weakly-ionised discs (Armitage, 2011).

2.1.2 Eccentric disc dynamics

This global accretion disc model may be generalised to describe eccentric discs simply by changing the initial orbit equilibrium conditions. The initial orbital energy and angular momentum of a fluid parcel uniquely determines the eccentricity of the orbit. Consider a fluid parcel initially located at $r = \lambda$ with a specific orbital angular momentum $\ell = \sqrt{GM\lambda}$. Given a specific orbital energy equal to $\varepsilon = -GM/(2\lambda)$, the fluid parcel will take on a circular orbit; however, if the energy is increased to $\varepsilon = -(1-e^2)\, GM/(2\lambda)$, the orbit becomes eccentric with eccentricity e. Then to first order in e, the eccentricity appears as horizontal epicycles with frequency κ, which for a Keplerian disc, $\kappa = \Omega$.

Thus a particular orbit is uniquely described by the semilatus rectum, λ, along with the orbit eccentricity. This suggests a generalisation of polar coordinates, (r, ϕ), natural to eccentric discs, which was introduced by Ogilvie (2001). These eccentric orbital coordinates, (λ, ϕ), therefore can describe any point in the disc when the eccentricity,

$e(\lambda)$, and the longitude of pericentre, $\omega(\lambda)$, are also specified, and which are in general functions of λ. Because eccentric Keplerian orbits are ellipses, the transformation between polar and eccentric orbital coordinates is

$$r = \frac{\lambda}{1 + e\cos(\phi - \omega)} \tag{2.3}$$

The Jacobian for this coordinate transformation from cartesian into the eccentric orbital coordinates is then

$$J(\lambda, \phi, z) = \frac{\partial(x, y, z)}{\partial(\lambda, \phi, z)} = \frac{\lambda\left(1 + (e - \lambda e')\cos\theta - \lambda e\omega'\sin\theta\right)}{(1 + e\cos\theta)^3} \tag{2.4}$$

where e' and ω' are the eccentricity gradient and orbital phase shift (or disc twistedness), respectively. $\theta = \phi - \omega$ here is the true anomaly, measuring the angular distance from pericentre. The Riemannian metric tensor, g_{ij}, and symmetric Levi-Civita connection, Γ^i_{jk} describe the vector calculus on this Riemannian manifold, and were first derived for the orbital coordinates by Ogilvie (2001). All relevant geometric quantities are reproduced in Appendix A for convenience.

With the geometry now defined in the orbital coordinate system, the invariant form of the Euler equations in a gravitational potential can be written as

$$D\rho = -\frac{\rho}{J}\partial_i(Ju^i) \tag{2.5a}$$

$$Du^i + \Gamma^i_{jk}u^j u^k = -g^{ij}\left(\partial_j\Phi + \frac{1}{\rho}\partial_j p\right) \tag{2.5b}$$

$$Dp = -\frac{\gamma p}{J}\partial_i(Ju^i), \tag{2.5c}$$

where $D = \partial_t + u^i\partial_i$ is the Lagrangian derivative, u^i is the typical contravariant velocity in the orbital coordinates, and Φ is the gravitational potential. An ideal gas equation of state, $p = (\gamma - 1)\, e$, was assumed to write equation (2.5c) in terms of pressure, providing closure. Index notation with assumed summation over repeated indices is used to write (2.5) succinctly. The additional connection terms in equation (2.5b) come from the covariant derivative in a general geometry, and will give rise to the Coriolis terms when entering a local frame.

2.1.3 Eccentric Lindblad resonance

Mean-motion orbital resonances are a well-studied mechanism that are able to continually increase orbit eccentricity, warranting this investigation into eccentric accretion

discs. This natural resonance occurs wherever the companion orbital period and local particle orbital period are commensurate (i.e. in a ratio of two small integers). At risk of oversimplification to construct a toy model in order to gain insight into this resonance, the circular restricted 3-body problem may be approximated by adding an ad-hoc gravitational term to the effective potential in the 1D equation of motion describing the orbital motion of a test particle in an axisymmetric potential:

$$\ddot{r} = -\partial_r \Phi_{\text{eff}} \tag{2.6}$$

where the effective potential for the 2-body system in the rotating frame is

$$\Phi_{\text{eff}}(r) = -\frac{GM}{r} + \frac{1}{2}\Omega^2 r^2. \tag{2.7}$$

The additional time-dependent potential term from the perturbing companion object can be constructed by analogy to an impulse model as

$$\partial_r \Phi_c \approx -\frac{GM_c}{r - R_c}\cos\Theta \tag{2.8}$$

where $\Theta \approx (\Omega_0 - \Omega_c)t$ is the angular separation of the test particle and the perturbing companion. An expansion, $r = \delta r + R_0$, can then be made for small perturbations from the initially nearly circular orbit, giving

$$\ddot{\delta r} \approx -\delta r \partial_{rr}\Phi_{\text{eff}}(R_0) \tag{2.9}$$

$$\approx -\delta r\left[\Omega_0^2 - \frac{2GM_c}{(R_c - R_0)^3}\cos\left((\Omega_0 - \Omega_c)t\right)\right]. \tag{2.10}$$

In the absence of the companion, the solution of (2.10) describes epicyclic oscillations with frequency $\kappa = \Omega_0$, but in general are written as $\kappa^2 = \partial_{rr}\Phi_{\text{eff}}$.

The form of equation (2.10) is that of the Mathieu equation,

$$\ddot{x}(t) + (a - 2q\cos(2t))\,x(t) = 0, \tag{2.11}$$

which generically produces parametric resonance at integer values of $\sqrt{a}$ for small values of the parametric excitation coefficient, q. To see why this is, a first order expansion about $q = 0$ is made, given the free-oscillatory zero order solution, $x_0(t) = A\cos(\sqrt{a}t)$. Moving the parametric oscillation term to the right side, and using $x_0(t)$,

the Mathieu equation now appears as a forced oscillator,

$$\ddot{x}(t) + ax(t) \approx qA\left[\cos\left((2-\sqrt{a})t\right) + \cos\left((2+\sqrt{a})\,t\right)\right. . \tag{2.12}$$

It is evident then that the primary resonance condition is $2-\sqrt{a}=\sqrt{a}$, giving the first parametrically unstable mode, $a=1$.

Comparing (2.12) and (2.10), the parameter a can be shown to be

$$\sqrt{a} = \frac{\Omega_0}{\Omega_0 - \Omega_c} \tag{2.13}$$

giving each of the parametrically unstable, mean-motion resonances for $m \in \mathbb{N}$:

$$\Omega_c = \left(1 \pm \frac{2}{m}\right)\Omega_0. \tag{2.14}$$

Thus, by periodically modulating the epicyclic frequency, the test orbit becomes parametrically resonant. It can be seen in the inertial frame that when this condition is met, the test particle traces closed orbits forming increasingly intricate rosettes for large m.

In generalising to a fluid disc, these mean-motion resonances take a different form due to continuum restrictions which limit the propagation of perturbations in certain regions of the disc, and prevents an explicit parametric resonance as previously demonstrated. Density waves of a given azimuthal pattern speed, ω_ϕ, can only freely propagate outside of the inner/outer Lindblad radii, where the magnitude of the wave frequency exceeds the epicyclic frequency in the co-orbiting frame. Thus $|\omega_\phi - \Omega| > \kappa$, which for a Keplerian disc only permits undamped frequencies greater than twice the local orbital frequency. Inside this "corotation" region, the particular azimuthal wave frequency nearly vanishes in a local frame and produces damped evanescent density waves (as the eigenvalues take on an imaginary component). Mean-motion resonances with $\omega_\phi = \Omega_c$ due to tidal forcing, and which occur between the Lindblad radii, then produce evanescent wave solutions that may generate long-time growth by secular interactions. Away from corotation, however, a Lindblad resonance is produced which generates density waves. When coupled with the eccentric mode (i.e. the first azimuthal inertial mode) of a fluid disc and with some means of dissipating the generated density waves, irreversible orbit eccentricity growth ensues (Lubow, 1991). The first of these Lindblad resonances to be encountered by an expanding disc is the $m=3$ (3:1) inner resonance, which is also the only eccentric Lindblad resonance not coincident with a corotation resonance. However, only binary systems with large mass ratios and

an extensive circumstellar disc are able to reach this resonance, making it a leading theory to explain the superhump phenomenon in Cataclysmic Binaries. Still, there is no known means of saturating this particular mean-motion resonance, motivating the development of the following local model for eccentric discs to investigate how the local dissipation of inertial waves might saturate this eccentricity growth.

2.2 Local disc models

2.2.1 Cartesian geometry

For studying *local* small-scale phenomena, it is numerically and often analytically beneficial to enter a local reference frame co-rotating and shearing with the disc (Goldreich and Lynden-Bell, 1965). It is conceptually easier to first develop the local model for a circular disc resulting in a cartesian metric and then draw analogies to the local eccentric model. In local cartesian coordinates, $(x, y, z) = (r - R_0, R_0 (\phi - \phi_0 - \Omega_0 t), z)$, centred about a fiducial radius, R_0, and co-rotating with the orbital frequency, $\Omega_0 = \Omega(R_0)$, additional symmetries are introduced which can greatly simplify analysis (see Figure 2.1). The equation of motion governing $\mathbf{u}$ in the rotating frame is found by transforming equation (2.5b), and using the cartesian metric with familiar definitions for the inner product:

$$\rho \left(D\mathbf{u} + 2\Omega_0 \hat{\mathbf{z}} \times \mathbf{u} \right) = -\nabla p - \rho \nabla \Phi_t, \tag{2.15}$$

where $\Phi_t = \Phi_c + \Phi_g$ is the effective tidal potential — the sum of the centrifugal potential arising from the non-inertial reference frame and the gravitational potential, respectively. The Keplerian rotation profile, $\Omega_k = \sqrt{GM/r^3}$ is independent of ϕ in this case of a circular disc.

The shearing box approximation is derived by expanding (2.15) in $\mathbf{x}/R_0 \ll 1$. The tidal potential in the local coordinates is then

$$\Phi_{\text{eff}} = -\frac{GM}{\sqrt{r^2 + z^2}} + \frac{1}{2}\Omega_0^2 r^2 = -q\Omega_0^2 x^2 + \frac{1}{2}\Omega_0^2 z^2 + \mathcal{O}\left(x^3 + z^3\right), \tag{2.16}$$

where the shear rate, $q \equiv -r \mathrm{d}\Omega/\mathrm{d}r$, measures the strength of differential rotation, which is 3/2 for a Keplerian disc. This expansion can be seen as a projection removing the curvature of the solution by eliminating dependence on y. Using this expansion with (2.15), the local shearing box approximation in primitive variables can be written

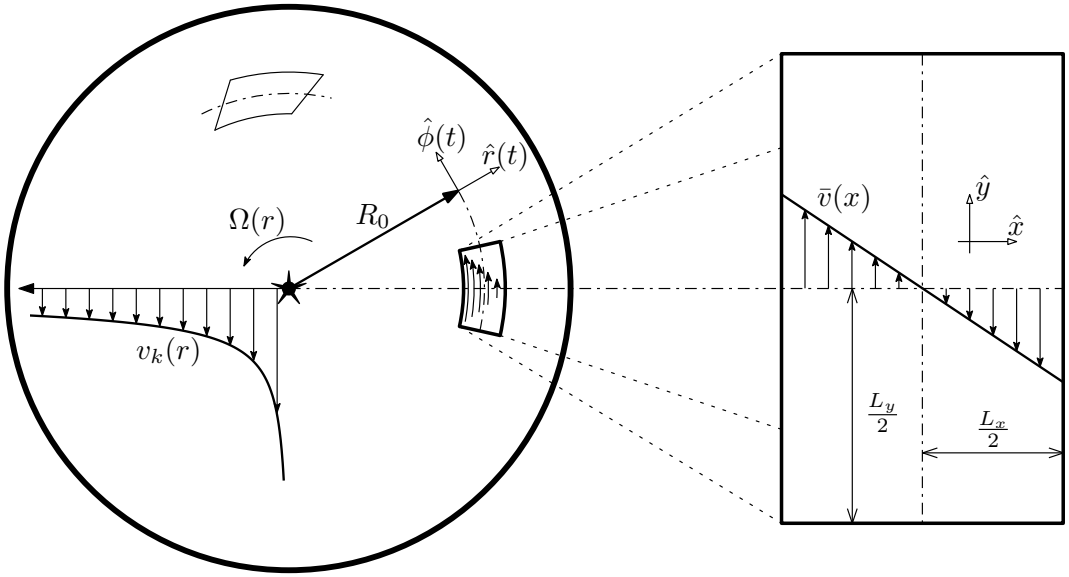

Fig. 2.1 The global disc (left) and extracted local cartesian patch (right). The control volume is shown sheared and advected at a later time while the shearing box remains unchanged.

as

$$D\rho = -\rho\nabla\cdot\mathbf{v} \tag{2.17a}$$

$$D\mathbf{v} = -\frac{1}{\rho}\nabla p - 2\Omega_0\hat{\mathbf{z}}\times\mathbf{v} + 2q\Omega_0^2 x\hat{\mathbf{x}} - \Omega_0^2 z\hat{\mathbf{z}} \tag{2.17b}$$

$$Dp = -\gamma p\nabla\cdot\mathbf{v}, \tag{2.17c}$$

where $\mathbf{v}$ is the relative velocity in local coordinates. An ideal gas equation of state, $p = (\gamma - 1)\, e$, is again assumed to write the energy equation in terms of pressure. The shearing box admits an equilibrium velocity solution, $\bar{\mathbf{v}} = -q\Omega_0 x\hat{\mathbf{y}}$, which is exactly the local uniform Keplerian orbital motion by construction. Additionally, for an initially isothermal (i.e. $\gamma = 1$) disc, the equilibrium density and pressure profiles are proportional to $\exp\left(-z^2/2H^2\right)$.

Simple periodic boundary conditions can be applied in the $\hat{\mathbf{y}}$ direction. Writing the vector of primitive variables as $\mathbf{W} = (\rho, \mathbf{v}, p)^T$, the boundary condition is explicitly

$$\mathbf{W}(x, y, z, t) = \mathbf{W}(x, y \pm L_y, z, t) \tag{2.18}$$

for a domain of size (L_x, L_y). However, this periodic boundary condition conflicts with the background Keplerian shear flow solution when applied in the $\hat{\mathbf{x}}$ direction. The $x = -L_x/2$ boundary is moving faster than at $x = +L_x/2$ by $v_{\text{boost}} = q\Omega_0 L_x$, and

so the velocity must be Galilean boosted and shifted in the $\hat{\mathbf{y}}$ direction to remain continuous. Finally, the boundaries in the vertical ($\hat{\mathbf{z}}$) direction must be chosen to approximate a vertically unbounded disc. Considering the vertical equilibrium profile, reflective boundary conditions are a good choice when enforced at a height $L_z/2 \gg H$ so as to minimise artificially constraining the fluid near the midplane.

A number of symmetries arise as consequence of making the shearing sheet approximation with these boundary conditions. The system (2.17) is evidently (globally) horizontally invariant — the dynamics are independent of the (r, ϕ) coordinates considered to be the centre of the domain, since these were neglected at leading order in the expansions. This also implies the direction towards the central gravitating object is ambiguous. Therefore, this local model is limited in determining global disc properties such as accretion rate or evolution of eccentricity *directly* (Regev and Umurhan, 2008). To deduce these properties, additional assumptions must be made about the radial disc structure.

2.2.2 Eccentric geometry

Analogous to the local cartesian approximation, the velocities in equation (2.5) are decomposed into the background orbital motion, with $u^\phi = \Omega(\lambda, \phi)$, and the relative velocities, v^i, so that $(u^\lambda, u^\phi, u^z) = (v^\lambda, \Omega + v^\phi, v^z)$. The global orbital coordinates are then expanded around a co-orbiting fiducial orbit, λ_0, centred on the midplane at $\varphi(t)$, and rotating with the disc at orbital frequency $\Omega(\lambda_0, \phi)$. These local non-orthogonal coordinates are $(\xi, \eta, z) = (\lambda - \lambda_0, \phi - \varphi(t), z)$, as shown at two different times in Figure 2.2.

2.2.2.1 Governing equations

The linear theory of Barker and Ogilvie (2014) has shown that the fastest growing azimuthal mode of the eccentric instability is the zero mode. Thus the local model given by Ogilvie and Barker (2014) can be further simplified by taking all $\partial_\eta \to 0$. However, the generally non-orthogonal coordinate system means that a component of the $\partial_\xi p$ remains in the $\hat{\eta}$-momentum equation, and so it cannot simply be passively advected as in the cartesian shearing box of §2.2.1. The governing equations describing the *local* (non-shearing) axisymmetric model of an eccentric disc in primitive variables

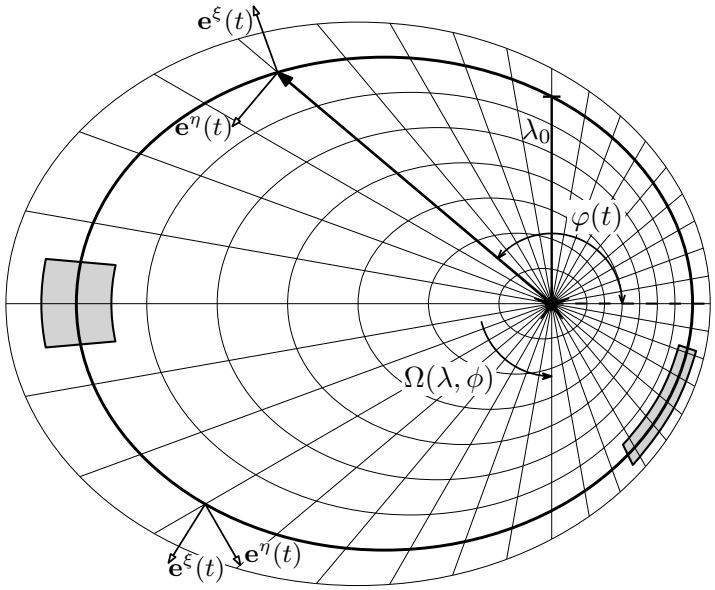

Fig. 2.2 The global orbital coordinate grid, (λ, ϕ), shown overlaid on the disc. The fiducial orbit, λ_0, is shown in bold along with the local contravariant basis vectors, $(\mathbf{e}^{\xi}, \mathbf{e}^{\eta})$, at two different times. The initial shearing box control volume at apocentre is shown stretched and advected at a later time.

are then

$$D\rho = -\rho(\Delta + \partial_\xi v^\xi + \partial_z v^z) \tag{2.19a}$$

$$Dv^\xi = -\frac{1}{\rho} g^{\lambda\lambda}\partial_\xi p - 2\Gamma^\lambda_{\lambda\phi}\Omega v^\xi - 2\Gamma^\lambda_{\phi\phi}\Omega v^\eta \tag{2.19b}$$

$$Dv^\eta = -\frac{1}{\rho} g^{\lambda\phi}\partial_\xi p - (\Omega_\lambda + 2\Gamma^\phi_{\lambda\phi}\Omega)v^\xi - (\Omega_\phi + 2\Gamma^\phi_{\phi\phi}\Omega)v^\eta \tag{2.19c}$$

$$Dv^z = -\Phi_2 z - \frac{1}{\rho}\partial_z p \tag{2.19d}$$

$$Dp = -\gamma p(\Delta + \partial_\xi v^\xi + \partial_z v^z), \tag{2.19e}$$

where the axisymmetric Lagrangian derivative is

$$D = \partial_t + v^\xi \partial_\xi + v^z \partial_z. \tag{2.20}$$

Apart from the cross-over pressure gradient terms due to the in-plane coordinates being non-orthogonal, and the Coriolis terms coming from the connection terms of the covariant derivative with u^ϕ, two additional forcing terms arise when considering the eccentricity. First, it is apparent that the effective tidal potential expansion now

varies with ϕ. Expanding the tidal potential similarly to the cylindrical case, but with $R(\theta) = \lambda_0/(1 + e\cos\theta)$, the second order term (in z) appearing in the local approximation is

$$\Phi_2 = \frac{GM}{\lambda_0^3}(1 + e\cos\theta)^3, \tag{2.21}$$

which is an implicit function of t, periodic with the eccentric orbital period,

$$\mathcal{P} = 2\pi\sqrt{\frac{\lambda_0^3}{GM}}\left(1 - e^2\right)^{-3/2}. \tag{2.22}$$

This is a periodic variation in the vertical gravitational acceleration due to the time-varying radius while on a constant orbit, λ_0.

A second modification to the cylindrical shearing box originates in the oscillatory geometry of the disc. Although the vertical ($\hat{\mathbf{z}}$) direction remains unchanged in the transformation, each of the velocity divergence terms in (2.17a) and (2.17c) must be transformed into the new coordinate system, and are non-zero due to the azimuthal velocity of the fiducial orbit, $\mathrm{d}\varphi/\mathrm{d}t = \Omega$. Accounting for this horizontal velocity divergence amounts to including an additional energy and mass source to the governing equations. Using the Jacobian, $J(\lambda_0, \phi, 0)$, for the eccentric orbital coordinates, this velocity divergence on the λ_0 orbit can be expressed as

$$\Delta = \frac{1}{J}\frac{\partial}{\partial\phi}(J\Omega) = \sqrt{\frac{GM}{\lambda_0^3}}\frac{\lambda_0(1 + e\cos\theta)\left(e'\sin\theta - e\omega'(\cos\theta + e)\right)}{1 + (e - \lambda_0 e')\cos\theta - \lambda_0 e\omega'\sin\theta}. \tag{2.23}$$

This is again an implicit periodic function of time, with period $\mathcal{P}$, which arises from the misalignment of the apse lines in the disc (ω') in addition to the non-constant eccentricity (e'). The orbits illustrated in Figure 2.2 show this orbital convergence near pericentre, as well as the azimuthal elongation of the local domain between apocentre and just before pericentre due to the relative azimuthal acceleration of points on the same orbit.

While the axisymmetric model presented above is quite general, as is that developed by Ogilvie and Barker (2014), the following work will be limited to $e' = \omega' = 0$ for isothermal discs. This greatly simplifies the following initial investigation into the nonlinear evolution by reducing the number of disc control parameters from three down to only the eccentricity.

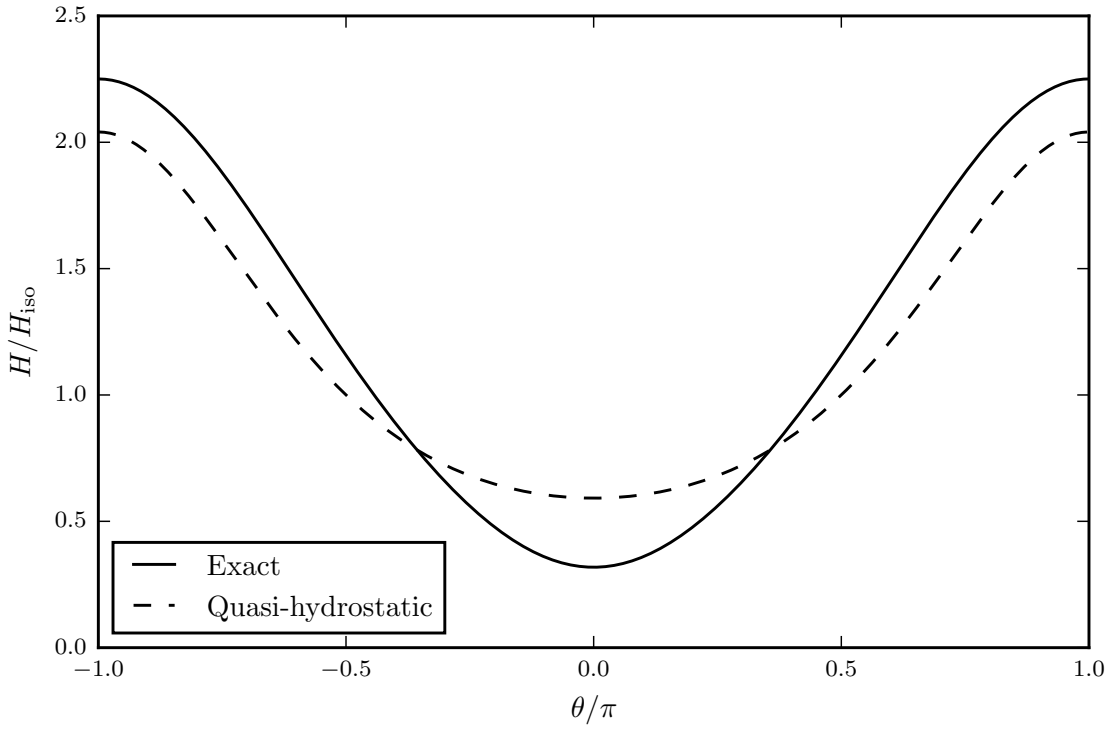

Fig. 2.3 Comparison of the resonant, laminar solution with the naïve solution which uses the hydrostatic scale height at each orbital radius, for $e = 0.3$.

2.2.2.2 Semi-analytic horizontally invariant laminar solution

The system of equations (2.19) admits laminar solutions that are horizontally invariant in the disc when $v^\xi = v^\eta = 0$. The system (2.19) then reduces to a set of three equations which may be solved for semi-analytically in the case of isothermal thermodynamics.

A naïve quasi-hydrostatic approach to solving the resulting 1D system might involve finding the isothermal scale height for a cylindrical disc at radius $R(\theta) = \lambda_0/(1+e\cos\theta)$ as it varies about the orbit. Although incorrect due to neglecting all dynamics of the system, it is still instructive for demonstrating the dynamical amplification (shown in Figure 2.3 for a disc with $e = 0.3$).

A semi-analytic solution becomes possible after noticing the eccentric forcing terms generate homogeneous vertical oscillations with period $\mathcal{P}$. The primitive variables are rewritten to uncouple the temporal and spatial dependencies by exploiting the solution

form of the homogeneous oscillations,

$$\rho(t,z) = \hat{\rho}(t)\mathrm{e}^{-\zeta^2/2} \tag{2.24a}$$

$$v^z(t,z) = \hat{v}^z(t)z \tag{2.24b}$$

$$p(t,z) = \hat{p}(t)\mathrm{e}^{-\zeta^2/2} \tag{2.24c}$$

where the similarity variable, $\zeta(t) = z/H(t)$, can be defined for an isothermal disc. The governing equations are then uncoupled by inserting this form for the primitive variables into (2.19):

$$\frac{\dot{\hat{\rho}}}{\hat{\rho}} - \frac{H}{\dot{H}}\zeta^2 - \hat{v}^z\zeta^2 = -(\Delta + \hat{v}_z) \tag{2.25a}$$

$$\dot{\hat{v}}^z + (\hat{v}^z)^2 = -\Phi_2 + \frac{c_s^2}{H^2}, \tag{2.25b}$$

where the redundant pressure equation is dropped. However, since the additional variable $H(t)$ has been introduced, a final relation is needed to close the system. This is found using a global mass conservation argument motivated by the mass component (2.19a). Integrating this term vertically over the disc, and using the form (2.24a), the closing equation is

$$\frac{\dot{\hat{\rho}}}{\hat{\rho}} + \frac{\dot{H}}{H} = -\Delta. \tag{2.26}$$

This set now can be simplified in terms of H, giving a second order non-linear ODE describing the evolution of H:

$$\ddot{H} = -\Phi_2 H + \frac{c_s^2}{H}. \tag{2.27}$$

This ODE describes a non-linear oscillator periodically forced by Φ_2, and admits both free oscillations as well as the forced response driven at the orbital frequency. The purely forced response can then be obtained by writing this as a periodic boundary value problem that can be solved numerically for H, and for which $\hat{\rho}$, $\hat{v}_z$, and $\hat{p}$ easily follow.

Thus in a local model, an eccentric disc exhibits a vertical oscillatory "breathing" mode, where the disc scale height periodically expands and contracts. Nonetheless, these solutions appear stationary in the inertial frame and therefore describe the global steady state of the eccentric disc. Figure 2.4 shows the vertical disc profile exhibiting this oscillation with equally spaced snapshots in time, starting (from the bottom) at apocentre, and displaying a large thin compression at pericentre. It is this vertical

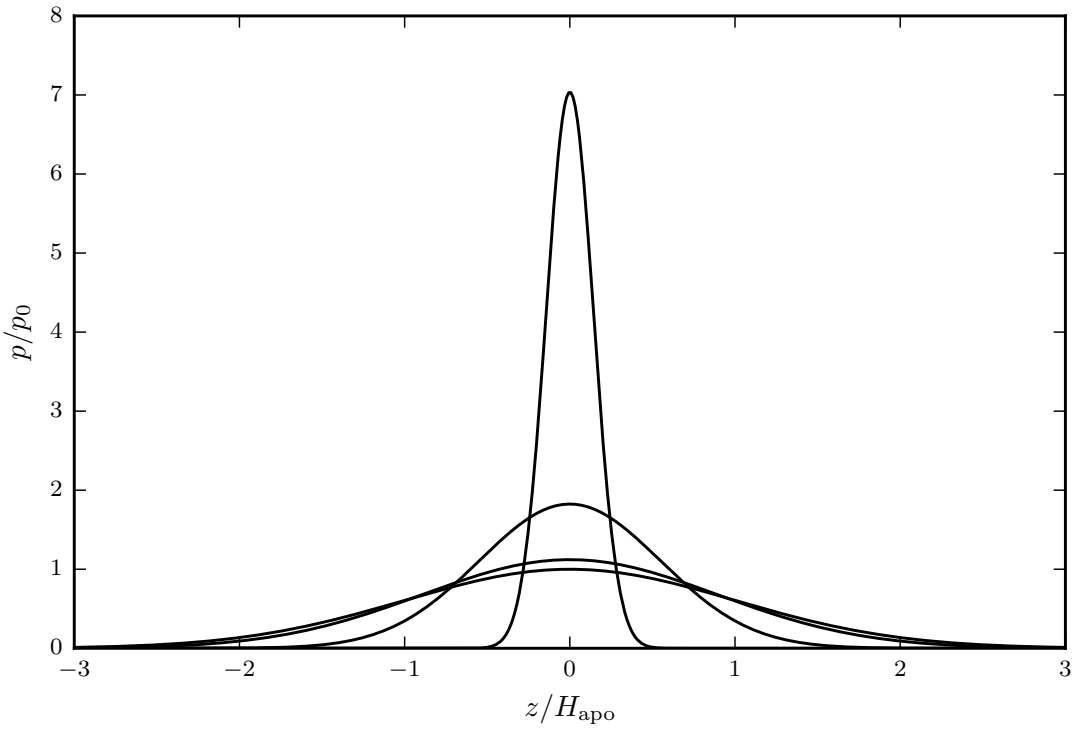

Fig. 2.4 Vertical pressure profiles demonstrating the laminar "breathing" mode, taken at four equally-spaced times between pericentre (top) and apocentre (bottom) for a disc with $e = 0.3$.

oscillation mode that parametrically couples with inertial waves, causing resonant instability.

2.2.2.3 Turbulent transport

It is now of interest to deduce the mass and angular momentum transport rates for the global disc represented by this local model. The angular momentum transport is often parameterised by the α-viscosity parameter (Shakura and Sunyaev, 1973), which posits that the efficiency with which angular momentum can be transported through the disc is proportional to the local averaged pressure. Thus α nondimensionalises the in-plane shear stresses responsible for transport with the average pressure, and for Keplerian shear is

$$\alpha = -\frac{2}{3}\frac{T^{r\phi}}{p}. \tag{2.28}$$

As explicit viscous stresses are not considered here, the specific angular momentum of each fluid parcel is conserved around an orbit. Thus the only source of α can be seen

as being attributed to some enhanced turbulent viscosity acting on the background shear,

$$\nu_T \sim \frac{\alpha c_s^2}{\Omega}. \tag{2.29}$$

In a turbulent state, this mixing is given by the Reynolds stresses,

$$T_R^{ij} = -\left\langle \rho v^i v^j \right\rangle, \tag{2.30}$$

where $< \cdot >$ indicates a time-average. This turbulent stress is an averaged stress arising from correlated velocity fluctuations, and which often greatly exceed viscous stresses in developed turbulence. Ignoring the viscous stresses, the total stress can be written for a general geometry,

$$T^{ij} = -\left\langle \rho v^i v^j \right\rangle - g^{ij} p \tag{2.31}$$

where it should be noted that for a general non-cartesian metric (and in orbital coordinates), there is an off-diagonal pressure contribution to the shear.

The in-plane shear stress, $T^{\lambda\phi}$, is the component responsible for turbulent transport of angular momentum. The net effect of this shear stress in the eccentric disc may be found by integrating the internal torque due to the shear stress and the total pressure over the entire disc, giving the α-viscosity in the local eccentric model,

$$\alpha = -\frac{\iint J R^2 T^{\lambda\phi} \Omega \, \mathrm{d}t \, \mathrm{d}z}{\iint J \lambda_0 p \Omega \, \mathrm{d}t \, \mathrm{d}z}, \tag{2.32}$$

which scales with the turbulent viscosity as expected.

2.2.2.4 Eccentricity evolution

Once a sustained turbulent state is achieved in the local model, it is then necessary to determine the induced eccentricity decay rate in order to balance the eccentricity growth from mean-motion resonances and find a stable eccentricity. This is not as simple as equating the dissipation of turbulent energy with an orbital energy decrease, consequently producing eccentricity decay. Depending on the phase of stresses in the orbit, the dissipation of perturbation energy may either decrease the angular momentum of the disc (thereby increasing eccentricity), or reduce the orbital energy (decreasing eccentricity).

Equation (52) in Ogilvie and Barker (2014) describes the precession and evolution of the global disc eccentricity, but which requires the mean quasi-radial velocity through the disc in order to solve. Given $e' = \lambda' = 0$ in a non-precessing disc, the eccentricity

decay rate may be simplified to

$$\ell\mathcal{M}\partial_t e = \iint \Big[2\left(\cos\theta + e\right)\partial_\lambda\left(JR^2T^{\lambda\phi}\right) - \frac{JR^2}{\lambda}\left(\cos\theta + e\right)T^{\lambda\phi} + \lambda\sin\theta\,\partial_\lambda\left(JR_\lambda T^{\lambda\lambda}\right) + JR^2\sin\theta\,T^{\phi\phi}\Big]\,\mathrm{d}\theta\,\mathrm{d}z, \tag{2.33}$$

where $\ell = \lambda_0^2\Omega_0$ is the specific angular momentum on the fiducial orbit, and $\mathcal{M} = \iint J\rho\Omega\,\mathrm{d}t\,\mathrm{d}z$ is the total mass of the disc. In order to evaluate the λ derivatives, additional approximations about the radial disc structure must be made. A global steady-state alpha disc model with constant α is often used to describe accretion discs, and is likely a good approximation for discs in Cataclysmic Binaries (Shakura and Sunyaev, 1973). This model produces a flared disc with surface density scaling $\Sigma \propto r^{-3/4}$, and vertically-integrated pressure $P \propto r^{-3/2}$. This same model was assumed in the work by Lubow (2010) to find the eccentricity growth rate in tidally distorted discs, and so will be used here to facilitate comparison to the eccentricity decay rate. Another simple self-similar model for an accretion disc with a constant aspect ratio, $\Sigma \propto r^{-5/2}$, and the same scaling for P as the alpha disc, may also be a reasonable model.

The integral of the Reynolds stresses may be found to scale with λ similar to P, allowing the λ derivatives to be calculated, giving

$$\ell\mathcal{M}\partial_t e = \iint J\sin\theta\left(-\frac{1}{2}R_\lambda T^{\lambda\lambda} + R^2T^{\phi\phi}\right)\Omega\,\mathrm{d}t\,\mathrm{d}z. \tag{2.34}$$

Thus for this alpha disc model, the in-plane shear stresses cancel and so the eccentricity evolution is dictated only by the ξ and η normal stresses varying around the disc.

It is expected that the α-viscosity and eccentricity decay are greatly influenced by the nature of the sustained turbulence. This steady turbulent state sourced by the nonlinear breaking of inertial waves will now be considered.

2.3 Inertial-acoustic waves

2.3.1 Background

Internal waves are propagating disturbances whose restoring force may be gravity or Coriolis, and which are permitted to propagate within a fluid by some stable density stratification or rotation. In a rotating frame, and where the dynamics are slow

compared to the orbital frequency, inertia-gravity waves are supported due to the influence of the Coriolis force. These inertial ("epicyclic") waves freely propagate only at particular frequencies depending on the spatial structure of the perturbation. This is described by the dispersion relationship, which gives the eigenvalues for axisymmetric perturbations of the form

$$\hat{\delta}(z)\mathrm{e}^{\mathrm{i}k_\xi \xi - \mathrm{i}\omega t} \tag{2.35}$$

and may be found from a linear perturbation analysis of the governing equations in the local coordinates. The dispersion relation is then

$$(\omega^2 - n\Omega^2)(\omega^2 - \kappa^2) = \omega^2 k_\xi^2 c_s^2, \tag{2.36}$$

for $n \in \mathbb{Z}^+$ designating the mode. Figure 2.5 shows the viable solutions for the first four modes of the dispersion relation. Two distinct branches are evident for these "inertial-acoustic" waves in the limit of large k_ξ: The high frequency branch has an acoustic character in which $\omega/\Omega_0 \to k_\xi H$. In other words, these waves are non-dispersive and the phase speed $v_p = c_s$ similar to acoustic waves. In contrast, the low frequency branch appears as an inertial wave, which for large wavenumber gives $\omega/\Omega_0 \to \sqrt{n}/(k_\xi H)$

Finally, the vertical structure of the eigenmodes $\hat{\delta}(z)$ can be found in terms of Hermite polynomials (Ogilvie and Latter, 2013; Okazaki et al., 1987):

$$\hat{v}^\xi, \hat{v}^\eta, \hat{h} \propto \mathrm{He}_n\left(\frac{z}{H}\right) \tag{2.37a}$$

$$\hat{v}^z \propto \mathrm{He}_{n-1}\left(\frac{z}{H}\right) \tag{2.37b}$$

for each mode n. Here, $h = c_s^2 \ln(\rho/\rho_0)$ is the enthalpy, taking the place of pressure and density in the isothermal disc. For $n = 1$, the horizontal velocity normal modes are linearly increasing with height, whereas the vertical velocity amplitude is constant. This vertical structure of the perturbations and background stratification means that the perturbation energy quickly falls off away from the midplane, as shown in Figure 2.6. It is hypothesised that because the stratification constrains the perturbation energy to be localised near the mid-plane, the nonlinear development of the parametric instability will be significantly different than that found in Papaloizou (2005a). Without strong vertical stratification, as in the Earth's atmosphere and as approximated in Papaloizou (2005b), the perturbation energy is constant in z.

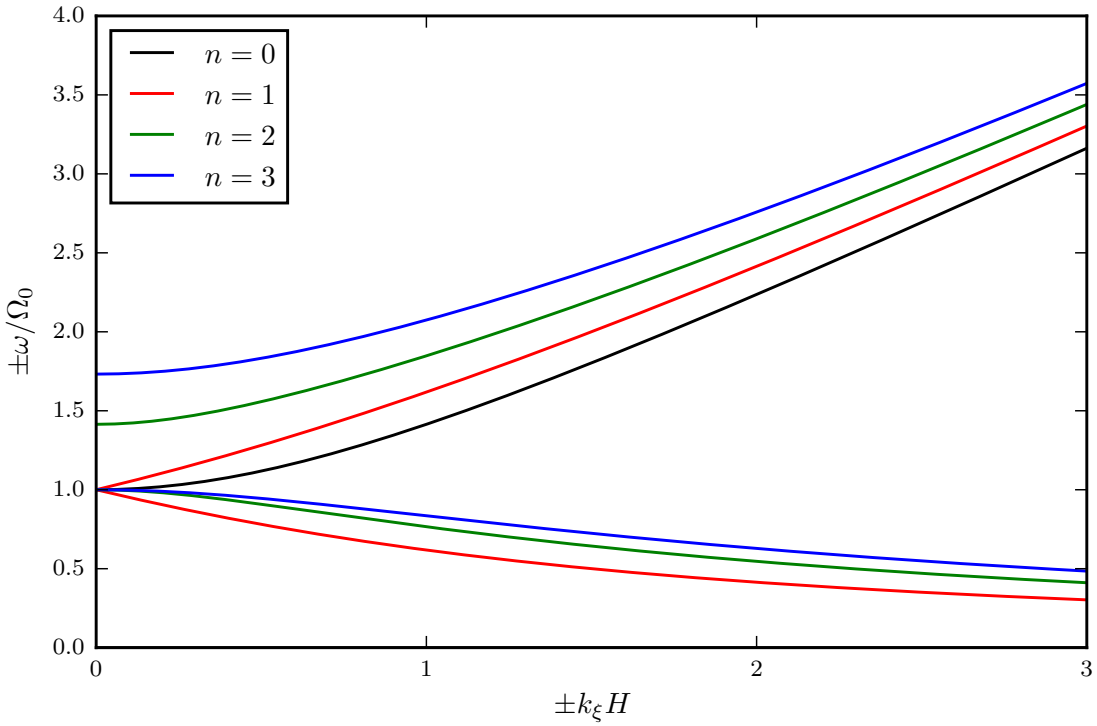

Fig. 2.5 Inertial-acoustic dispersion relationship (2.36) giving the viable freely propagating waves, $\omega(k_\xi)$, for the first four modes.

2.3.2 Parametric instability of inertial waves

Analogous to the eccentric parametric instability producing eccentricity growth in the global disc equations (§2.1.3), parametric resonance may be excited in the local model by the inherent modulation of the physical parameters including the orbital convergence of streamlines as well as the tidal potential, Φ_2, at a frequency Ω, due to the prescribed eccentricity. However, now the parametric driving frequency is set as Ω, and the natural oscillation frequencies of the inertial waves are selected, given the resonance condition

$$\omega = \frac{n}{2}\Omega. \tag{2.38}$$

The strongest ($n = 1$) resonance occurs then for inertial waves with frequency $\omega = {}^1\!/_2\Omega_0$, which corresponds to the wavenumber $k_\xi H = {}^1\!/_2\sqrt{3(4n-1)}$.

The founding linear instability analysis studying the growth of this parametric instability in constant eccentricity discs was carried out by Papaloizou (2005b). His local stability analysis applies only near the midplane where he makes the approximation of a cylindrical disc gravitational potential, $\Phi = -GM/r$, independent of z, such

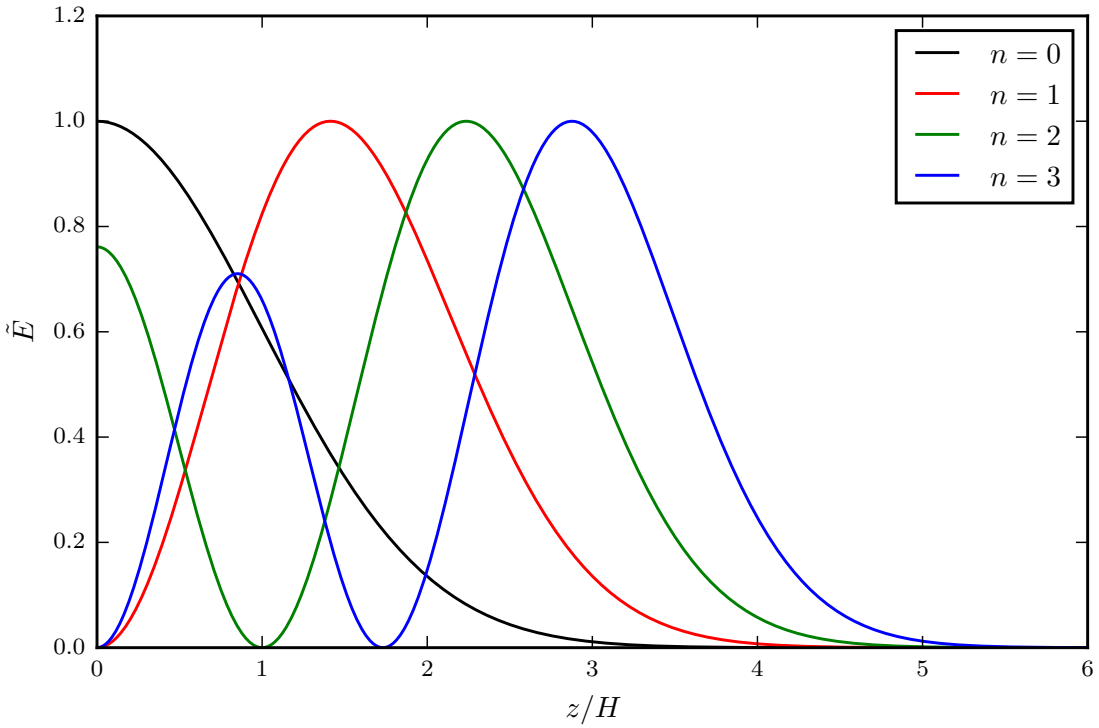

Fig. 2.6 Perturbation energy ($\rho v^i v^i$) for the first few inertial modes, showing the energy containment near the mid-plane.

that there is no vertical stratification. In the limit that $n, k_\xi \to \infty$ it was found that the oscillating divergence of the non-circular streamlines around the disc produces a growth rate of $\sigma = \frac{3}{16}e$. In follow-up nonlinear global simulations, Papaloizou (2005a) additionally finds small-scale subsonic turbulence as the instability saturates, leading to a slow decay of eccentricity. Barker and Ogilvie (2014) extended this initial linear theory to account for the vertical structure of the disc due to a spherical gravitational potential varying off of the mid-plane. They found that the effect of the enhanced vertical oscillations made possible by the vertical stratification contributes an additional free energy source to the parametric growth. Consequently a larger growth rate of $\sigma = \frac{3}{4}e$ is shown, compared to that with no vertical structure. This linear theory inevitably breaks down as the inertial waves grow too large. At that point, nonlinear effects become important, eventually causing the inertial waves to break.

2.3.3 Inertial wave breaking

A criterion for the critical amplitude at which inertial waves break will now be constructed, first by order of magnitude kinematic arguments, and then more physically-grounded in the stability of rotating fluids.

General waves are often seen breaking as their constituent particle velocities exceed the phase velocity, leading to steepening gradients. A similar argument could be made for inertial waves. Restricting the wavevector to be in the $\hat{\xi}$ direction, the inertial wave perturbations are then described by

$$\tilde{v} = \hat{v}\mathrm{e}^{\mathrm{i}(k_\xi \xi - \omega t)}. \tag{2.39}$$

The phase speed of this perturbation is $v_p = \omega/k_\xi$, suggesting that the critical velocity for breaking is $\hat{v}^\xi_{\mathrm{crit}} \approx \omega/k_\xi$.

A more physically-motivated argument can be constructed by suggesting that inertial waves break when they produce a local violation of the Rayleigh stability criterion — where the angular momentum gradient locally becomes negative,

$$\frac{\mathrm{d}\ell}{\mathrm{d}r} = \frac{\mathrm{d}}{\mathrm{d}r}\left(r^2|v^\phi|\right) < 0. \tag{2.40}$$

The angular momentum equation for collisionless particles in the local model is

$$\ell = R\tilde{v}^\eta + 2\Omega R\xi \tag{2.41}$$

where $\tilde{v}^\eta$ is the angular velocity perturbation from the local eccentric model. Equating the ξ derivative to 0, and using the fact that

$$\tilde{v}^\xi = \frac{1}{2}\frac{R\omega}{\Omega}\tilde{v}^\eta, \tag{2.42}$$

the same result is obtained that $\hat{v}^\xi_{\mathrm{crit}} \approx \omega/k_\xi$. Written in terms of the particle displacement, $\delta\xi$, shows that breaking occurs when $k_\xi \delta\xi \approx 1$.

Finally, the critical height above the mid-plane that the inertial waves will begin to break, is found to be

$$z_{\mathrm{crit}} = \frac{\omega}{k_\xi \hat{v}^\xi_0(1)}\mathrm{e}^{-\gamma t} \tag{2.43}$$

for the $n = 1$ mode of the profile given by (2.37), and for the growth rate γ. Thus looking far enough off of the mid-plane, the inertial waves can always be seen to break.

Without considering nonlinear effects, then as the parametric instability grows, the breaking region approaches the mid-plane if unbalanced by a secondary instability.

Although these criteria are motivated in a circular disc, they are found to be a good approximation for small eccentricities when compared to numerical simulations.

Chapter 3

Numerical methods

3.1 Finite volume methods

The finite volume methods (FVM) will first be developed in an inertial Cartesian frame before extending to a co-rotating frame of reference. The compressible Euler equations of ideal-gas hydrodynamics with a point-mass gravitational potential (2.5), are a hyperbolic set of equations with full real eigenvalues. Thus information travels across the domain at finite speed, and so the domain of dependence is a bounded set. The governing equations consequently lend well to explicit methods (including FVM) as well as domain decomposition for MPI parallelisation.

The finite volume methods will thus be employed to numerically solve the developed physical models cast in a general conservative form,

$$\partial_t \mathbf{U} + \nabla \cdot \mathbf{F}(\mathbf{U}) = \mathbf{S}(\mathbf{U}, t). \tag{3.1}$$

The governing equations must be cast into this conservation form, describing the vector of conserved variables, $\mathbf{U} = (\rho, \rho\mathbf{u}, E)^T$, in order to converge to the weak solution upon discretisation. This conservative construction guaranteeing the correct wave speeds is a particular strength of FVM over finite differences or elements in fluid dynamics, although generally more difficult to implement, and in particular for this problem.

3.1.1 Generalised finite volume formulation

An ideal numerical scheme is designed to emulate the properties and behaviour of the physics it is being used to model. The foremost of these properties is being conservative, and so the following methods will by construction be conservative.

The vector of physically conserved continuous variables, $\mathbf{U}(x, y, z, t)$, is discretised by interpreting the value at the cell-centred point, $\mathbf{U}_{ijk}(t) = \mathbf{U}(i\Delta x, j\Delta y, k\Delta z, t)$, to be averaged over the the whole of the ijk^{th} finite control volume (or area in 2D). This integral average over cell volume V_{ijk} is

$$\begin{aligned}\mathbf{U}_{ijk}(t) &= \frac{1}{V_{ijk}} \int_{z_{k-\frac{1}{2}}}^{z_{k+\frac{1}{2}}} \int_{y_{j-\frac{1}{2}}}^{y_{j+\frac{1}{2}}} \int_{x_{i-\frac{1}{2}}}^{x_{i+\frac{1}{2}}} \mathbf{U}(x, y, z, t)\, \mathrm{d}x\, \mathrm{d}y\, \mathrm{d}z \\ &= \frac{1}{V_{ijk}} \iiint_{V_{ijk}} \mathbf{U}(\mathbf{x}, t)\, \mathrm{d}\mathbf{V}. \end{aligned} \tag{3.2}$$

The finite volume method is then founded on locally enforcing a general conservation law (3.1) in each discretised control volume, V_{ijk}. Here $\mathbf{F}(\mathbf{U})$ is the *equation* flux function and $\mathbf{S}(\mathbf{U}, t)$ is the sourcing term, both mapping $\mathbb{R}^5 \to \mathbb{R}^5$ in the case of the 3D Euler system.

Integrating (3.1) over the finite volume, V_{ijk}, and using Leibniz's rule with the Gauss-Ostrogradsky theorem, gives an ODE describing the evolution of the finite volume as

$$\frac{\mathrm{d}}{\mathrm{d}t}\mathbf{U}_{ijk}(t) + \oiint_{\partial V_{ijk}} \mathbf{F}(\mathbf{U}) \cdot \mathrm{d}\mathbf{A} = \left(\mathbf{S}\left(\mathbf{U}, t\right)\right)_{ijk}. \tag{3.3}$$

The discretised finite volume source term is written here in the continuous form $(\mathbf{S}(\mathbf{U}, t))_{ijk} = \iiint_{V_{ijk}} \mathbf{S}(\mathbf{U}, t)\mathrm{d}\mathbf{V}$ to emphasise that the source term is volume-averaged. Often times the conservative set of equations define a flux function which is difficult to solve all at once. Thus, dimensional splitting algorithms help make the 3D update formula (3.3) computationally tractable.

3.1.2 Operator splitting

Operator splitting is often employed to simplify the full 3D non-homogeneous conservation law into a series of 1D fractional step operators without compromising solver accuracy. Thus only a generalised 1D finite volume scheme needs to be designed.

Using the Method of Lines the general conservation equation (3.1) can be spatially semi-discretised as

$$\frac{\mathrm{d}\mathbf{U}}{\mathrm{d}t} = A_x\mathbf{U} + A_y\mathbf{U} + A_z\mathbf{U} + A_s\mathbf{U} \tag{3.4}$$

where A_x, A_y, and A_z are the discrete operators for some approximation to the partial derivatives of $\mathbf{F}(\mathbf{U})$. A_s is the source function in the special case that it can be written as a linear operator on $\mathbf{U}$, which is now a vector of vectors containing all spatial data reordered into a single column. It is trivial to solve this ODE giving $\mathbf{U}(t)$ in each discrete control volume:

$$\mathbf{U} = \mathbf{U}_0 \mathrm{e}^{t(A_x+A_y+A_z+A_s)} \tag{3.5}$$

Matrix exponentials are not in general commutative and so this exponent cannot be written as the product of the individual exponents. However, to make an overall 2^{nd} order scheme, (3.4) only needs to be solved at 2^{nd} order itself!

Now considering just a 2D method with a source term, there are two 2^{nd} order methods to split the exponent in equation (3.5):

$$\mathrm{e}^{t(A_x+A_y+A_s)} = \mathrm{e}^{\frac{1}{2}tA_x}\mathrm{e}^{\frac{1}{2}tA_y}\mathrm{e}^{tA_s}\mathrm{e}^{\frac{1}{2}tA_y}\mathrm{e}^{\frac{1}{2}tA_x} + \mathcal{O}\left(t^3\right) \tag{3.6}$$

$$= \frac{1}{4}\left[\mathrm{e}^{tA_x}\mathrm{e}^{tA_y}\mathrm{e}^{tA_s} + \mathrm{e}^{tA_x}\mathrm{e}^{tA_s}\mathrm{e}^{tA_y} + \mathrm{e}^{tA_y}\mathrm{e}^{tA_s}\mathrm{e}^{tA_x} + \mathrm{e}^{tA_s}\mathrm{e}^{tA_y}\mathrm{e}^{tA_x}\right] + \mathcal{O}\left(t^3\right) \tag{3.7}$$

The first of these operator splitting methods is Strang splitting, which is implemented as a half time step in x then y, a full time step to solve the source with A_s, and finally the second half time step in y then x. The second method, (3.7), is the parallel splitting scheme, which gains 2^{nd} order accuracy by averaging each of the 4 cyclic permutations of the linear operators. However, it will be shown that taking two half steps is not exactly equivalent to taking one full step, solely because of compounding truncation errors. This compounding error often emerges as an increase in numerical diffusion with increasing number of time steps. Strang splitting decreases the effective time step by half and consequently increases the numerical diffusivity. Therefore, although parallel splitting is over twice as expensive, it is favoured over Strang splitting because it does not unnecessarily decrease the advection step size.

Now the 3D ODE given by equation (3.3) has been simplified to four independent 1D ODEs. Defining the solution operator in the $\hat{\mathbf{x}}$ direction, $\mathcal{L}_x^t$, which approximates (to within the constant of integration) the solution to

$$\partial_t \mathbf{U} + \partial_x \mathbf{F}(\mathbf{U}) = 0 \tag{3.8}$$

at time t for some initial condition $\mathbf{U}_0$, it is clear that, $\mathcal{L}_x^{\Delta t} = \exp(\Delta t A_x)$, by using the approximation to the discrete partial derivative and equation flux operator, A_x. A first order solution to the 3D system, (3.1), is then given by $\mathbf{U}^{n+1} = \mathcal{L}_x^{\Delta t}\mathcal{L}_y^{\Delta t}\mathcal{L}_z^{\Delta t}\mathcal{L}_s^{\Delta t}\mathbf{U}^n$.

The only task is to find each $\mathcal{L}^{\Delta t}$ to step $\mathbf{U}^n$ forward by Δt in a single dimension at a time.

Focussing on just the $\hat{\mathbf{x}}$ direction advection solution, $\mathcal{L}_x^{\Delta t}$, in 1D the closed surface integral term of equation (3.3) becomes a difference of fluxes evaluated at the cell edges, $x_{i\pm\frac{1}{2}}$. Integrating from time $n\Delta t$ to $(n+1)\Delta t$, gives the 1D conservative update formula,

$$\mathbf{U}_i^{n+1} = \mathbf{U}_i^n + \frac{\Delta t}{\Delta x}\left(\mathbf{f}_{i-\frac{1}{2}} - \mathbf{f}_{i+\frac{1}{2}}\right). \tag{3.9}$$

This allows the vector of conservative variables to be marched forward in time, given the time-averaged equation flux at each cell edge. This new flux is termed the *scheme*[2] flux, $\mathbf{f}_{i\pm\frac{1}{2}}$, which is the flux through the cell edges normal to the solution direction ($\hat{\mathbf{x}}$). It is clear now that this scheme is conservative, because the flux leaving one cell is identically the flux entering the adjacent cell.

Whereas the grid size Δx is specified by the user at run-time, the time step size in (3.9) must be adaptively chosen to help ensure numerical stability. The time step and cell size define a computational grid speed, $\Delta x/\Delta t$, which is the fastest speed that information such as waves, characteristics, or flow velocities can be resolved to travel across the computational domain. The grid velocity must be greater than the speed of the physics of interest to have stability. It is convenient to define the Courant-Friedrich-Lewy (CFL) number,

$$\mathrm{CFL} = \frac{\Delta t}{\Delta x} u_{\max} \tag{3.10}$$

where $u_{\max} = \max_{\forall i}(|u| + a)$ over all cells, and a is the sound speed in a numerical context. The CFL number is then the fraction of a cell width that is acceptable for a disturbance to propagate in a single time step. $\mathrm{CFL} \leq 1$ is a necessary condition for any finite volume method to be stable and convergent, though a particular scheme may further restrict the stable CFL regime. Throughout this work, $\mathrm{CFL} = 0.9$ will be used, except during the first 5 time steps when $u_{\max}$ is not known with enough certainty, and so CFL will be reduced to 0.2.

The final 2$^{\mathrm{nd}}$ order splitting scheme of choice for the 2D system with sourcing is

$$\mathbf{U}^{n+1} = \mathcal{L}_s^{\frac{1}{2}\Delta t} \frac{1}{2}\left(\mathcal{L}_x^{\Delta t}\mathcal{L}_y^{\Delta t} + \mathcal{L}_y^{\Delta t}\mathcal{L}_x^{\Delta t}\right)\mathcal{L}_s^{\frac{1}{2}\Delta t}\mathbf{U}^n. \tag{3.11}$$

The fractional steps are as follows: The source term is first stepped forward $\frac{1}{2}\Delta t$ using $\mathbf{U}^n$ as the initial condition. Then the x and y terms are stepped forward parallel in

[2]Not to be confused with the equation flux function, $\mathbf{F}(\mathbf{U})$.

time, using the output of $\mathcal{L}_s^{1/2\Delta t}\mathbf{U}^n$ as the initial condition. Finally, this output is used again as the input for the final half-step of the source term to give $\mathbf{U}^{n+1}$. This scheme was chosen to minimise numerical diffusivity and artificial anisotropies in the advection terms while avoiding the 2x penalty incurred by using parallel splitting on the source term.

3.1.3 Advection solver

With the full 3D advection step simplified into three uncoupled 1D steps, all that is left to do now is evaluate the scheme fluxes in the 1D conservative update (3.9) defining each solution operator, $\mathcal{L}$, in terms of the equation flux,

$$\mathbf{F}(\mathbf{U}) = \begin{pmatrix} \rho\mathbf{u} \\ \rho\mathbf{u}\mathbf{u} + p\mathrm{I} \\ (E+p)\mathbf{u} \end{pmatrix} \tag{3.12}$$

specific to the compressible Euler equations. For MUSCL-type "high-resolution" schemes which gain spatially 2nd order accuracy through domain reconstruction, the advection solution algorithm may be split into *reconstruct*, *solve*, and *average* steps which will be outlined in the following sections. This entails a 2nd order spatial reconstruction, followed by solving the generalised Riemann problem at each reconstructed cell edge, and finally employing a numerical integration scheme to average the solution over the advanced time step. Other 2nd order upwinding schemes that do not perform this spatial reconstruction (such as the Weighted-Area Flux scheme) will not be utilised here, but an in-depth comparison of which may be found in Wienkers (2016).

3.1.3.1 Reconstruction

A common technique for constructing a higher order method is to reconstruct the piecewise constant discrete data (3.2) to more accurately define the initial left and right cell edge states for the solution step. This is the idea behind MUSCL-type methods (Monotonic Upstream-centred Scheme for Conservation Laws). Specifically, to gain 2nd order spatial accuracy, the variables within each cell will be interpolated using a piecewise linear reconstruction (see Figure 3.1). So as to not bias one direction over the other, the slope is defined from a centred difference (Fromm), $\Delta_i = {}^1\!/_2(\mathbf{U}_{i+1} - \mathbf{U}_{i-1})$, and is a vector corresponding with the vector of conservatives. This slope can then be

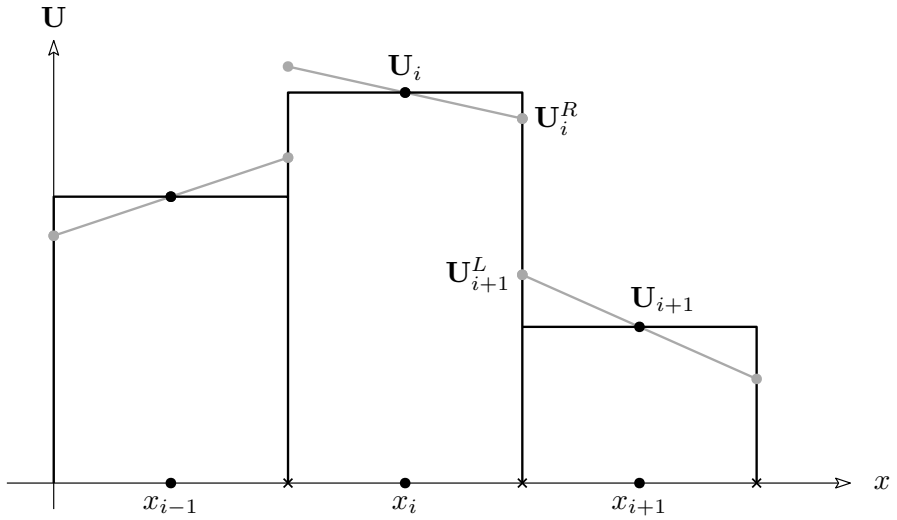

Fig. 3.1 MUSCL-type piecewise linear Fromm reconstruction (grey), of the initial piecewise constant data.

used to determine the boundary-extrapolated values at the left and right edges:

$$\begin{aligned} \mathbf{U}_i^L &= \mathbf{U}_i^n - {}^1\!/_2 \Delta_i \\ \mathbf{U}_i^R &= \mathbf{U}_i^n + {}^1\!/_2 \Delta_i. \end{aligned} \tag{3.13}$$

Slope limiting

An ideal 2nd order modified Godunov method is 2nd order everywhere the solution is smooth. These so-called "high resolution" schemes should be consistent, stable, and therefore convergent as well as being numerically inviscid and resolving discontinuities without artificial oscillations.

A metric for these oscillations inherent to higher order methods is the Total Variation. The Total Variation is defined as

$$\mathrm{TV}\left(\mathbf{U}^n\right) = \sum_{i=-\infty}^{\infty} |\mathbf{U}_{i+1}^n - \mathbf{U}_i^n|, \tag{3.14}$$

such that any spurious oscillations introduced into $\mathbf{U}^n$, however small, will increase the total variation. If the total variation is monotonically decreasing in time, then it is assured there are no oscillations near discontinuities. This total variation diminishing (TVD) property is a necessary requirement to construct a high resolution 2nd order scheme; however, Godunov (1959) proved that the highest order monotone (and therefore TVD) scheme is only 1st order! A constraint on 2nd order solutions must

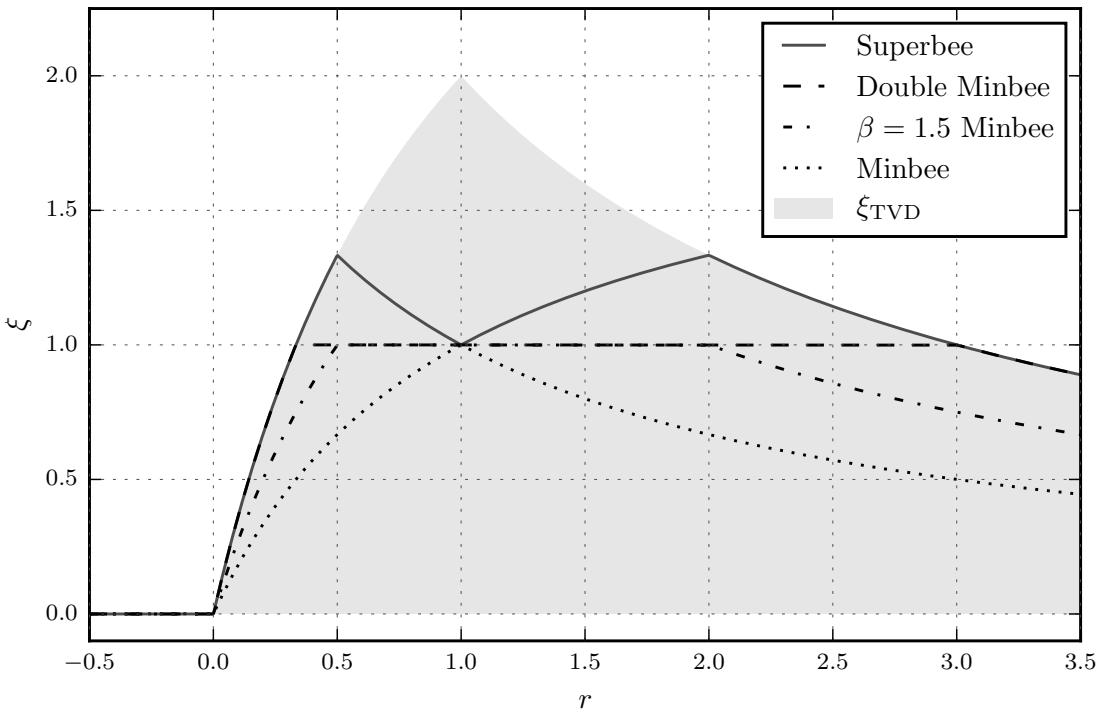

Fig. 3.2 The Superbee and Minbee slope limiter functions within the Sweby (1984) 2nd order TVD region (grey).

then be imposed to regain TVD. Limiting selectively suppresses the technique used to gain 2nd order, returning the scheme to the 1st order monotone scheme where the solution becomes steep, while maintaining higher-order accuracy in smooth regions. This "steepness" is given by

$$\mathbf{r}_i = \frac{\Delta \mathbf{U}_{i,\text{up}}}{\Delta \mathbf{U}_{i,\text{down}}} \tag{3.15}$$

which are the upwind and downwind differences of the entire state vector $\mathbf{U}$.

As the MUSCL acronym implies, the reconstruction is monotone and therefore TVD. The TVD constraint for MUSCL schemes is in the form of a limiter, $\xi(\mathbf{r})$, applied to the slope during reconstruction to mitigate spurious oscillations (as in the left edge of cell x_i in Figure 3.1), effectively increasing the numerical dissipation locally to smear out shocks. The limited slope, $\bar{\Delta}_i = \xi_i \Delta_i$, is instead used to determine the boundary-extrapolated values at the left and right edges.

The two limiter functions that will be used throughout this work are the Minbee and Double Minbee limiters, shown in Figure 3.2. Although the growth rate of the sensitive instability of interest is affected by numerical dissipation, it is more devastated

by phase errors which would accumulate over long evolution times introduced by antidiffusion (when $\xi > 1$) such as in the Superbee limiter. Superbee liberally attempts to compensate for any dissipation by artificially amplifying reconstructions with small r. The Minbee limiters do not artificially steepen the slope, and so only adds dissipation on strong discontinuities or shocks, while leaving everything else 2$^{\text{nd}}$ order ($\xi = 1$).

Well-balanced correction

A cursory implementation of the source splitting method in §3.1.2 produces significant numerical artefacts on the seemingly trivial problem of maintaining the vertical hydrostatic equilibrium solution (as pointed out in Slyz and Prendergast, 1999). This is because the hydrostatic pressure profile, which at cell interfaces manifests as a pressure jump, is interpreted by the Riemann solver as a propagating wave in the direction of the gradient of the potential. Even with 2$^{\text{nd}}$ order parallel source splitting, the advection terms are not exactly balanced with the source term, as it is analytically in

$$\frac{\partial p}{\partial z} = -\rho \frac{\partial \Phi}{\partial z}. \tag{3.16}$$

So-called "well-balanced" schemes (Greenberg and Leroux, 1996) exactly satisfy a discrete form of this equilibrium; however, often assuming some underlying thermodynamic equilibrium to do so (Botta et al., 2004; Chandrashekar and Klingenberg, 2015; LeVeque, 1997). The method introduced in Käppeli and Mishra (2016) rather relies on a simple pressure reconstruction and assumes no thermodynamic equilibrium. A modified 2$^{\text{nd}}$ order version of their technique is implemented here, which makes a slope-limited MUSCL-type reconstruction of the perturbation quantities, differing from the extrapolated pressure equilibrium in the neighbouring cell centres approximated as

$$\begin{aligned} p_i(x_{i-1}) &= p_i + \frac{\rho_{i-1} + \rho_i}{2} \frac{\Phi_i - \Phi_{i-1}}{\Delta z} \Delta z \\ p_i(x_{i+1}) &= p_i + \frac{\rho_i + \rho_{i+1}}{2} \frac{\Phi_{i+1} - \Phi_i}{\Delta z} \Delta z. \end{aligned} \tag{3.17}$$

The potential gradient must be calculated discretely so that this extrapolation satisfies the discrete pressure equilibrium defined as

$$\frac{p_{i+1} - p_i}{\Delta z} = -\frac{\rho_i + \rho_{i+1}}{2} \frac{\Phi_{i+1} - \Phi_i}{\Delta z}. \tag{3.18}$$

The MUSCL reconstruction step is instead approximated in primitive variables, with $\bar{\Delta}_i$ being the limited centred difference of the perturbation quantities. The reconstruction

(3.13) then gives the left and right edge states as

$$\begin{aligned} \mathbf{W}_i^L &= \mathbf{W}_i^n - 1/2 \left(\bar{\Delta}_i + \Delta_p^L \right) \\ \mathbf{W}_i^R &= \mathbf{W}_i^n + 1/2 \left(\bar{\Delta}_i + \Delta_p^R \right) \end{aligned} \tag{3.19}$$

where the pressure component of the limited slopes are supplemented with the equilibrium pressure difference at the cell edges,

$$\begin{aligned} \Delta_p^L &= -\rho_i \left(\Phi_i - \Phi_{i-1} \right) \\ \Delta_p^R &= -\rho_i \left(\Phi_{i+1} - \Phi_i \right). \end{aligned} \tag{3.20}$$

Thus for an arbitrary thermodynamic and hydrostatic equilibrium, this correction to the reconstruction maintains the steady state equilibrium to machine precision given that the potential gradient source term is unsplit from the integration scheme.

3.1.3.2 Riemann solution

The most common upwind methods for solving the compressible Euler equations are based on solving a Riemann problem at each intercell boundary arising from discretisation (see Figure 3.3a), to obtain the intercell scheme flux, $\mathbf{f}_{i\pm\frac{1}{2}}$. These general methods are called Godunov Methods. The resulting Riemann problem is in a family of generalised Riemann problems which describe any initial value problem to a conservation equation with a piecewise initial condition consisting of a single discontinuity. Thus at each cell edge, a Riemann problem arises due to the domain discretisation (3.2) described by the initial condition,

$$\mathbf{U}(x, t=0) = \begin{cases} \mathbf{U}_L & x \leq 0 \\ \mathbf{U}_R & x > 0 \end{cases} \tag{3.21}$$

which evolves according to the conservative advection terms of the governing equations (left hand side of (3.1)). Given a solution to this Riemann problem, the original (1^{st} order) Godunov upwind method evaluates the scheme flux using the state vector of the Riemann problem solution, $\check{\mathbf{U}}_{i+\frac{1}{2}}\left(\frac{x}{t}\right)$, at the cell edge (where $x = 0$ due to a translation by $x_{i+\frac{1}{2}}$), giving

$$\mathbf{f}_{i+\frac{1}{2}} = \mathbf{F}\left(\check{\mathbf{U}}_{i+\frac{1}{2}}(0) \right). \tag{3.22}$$

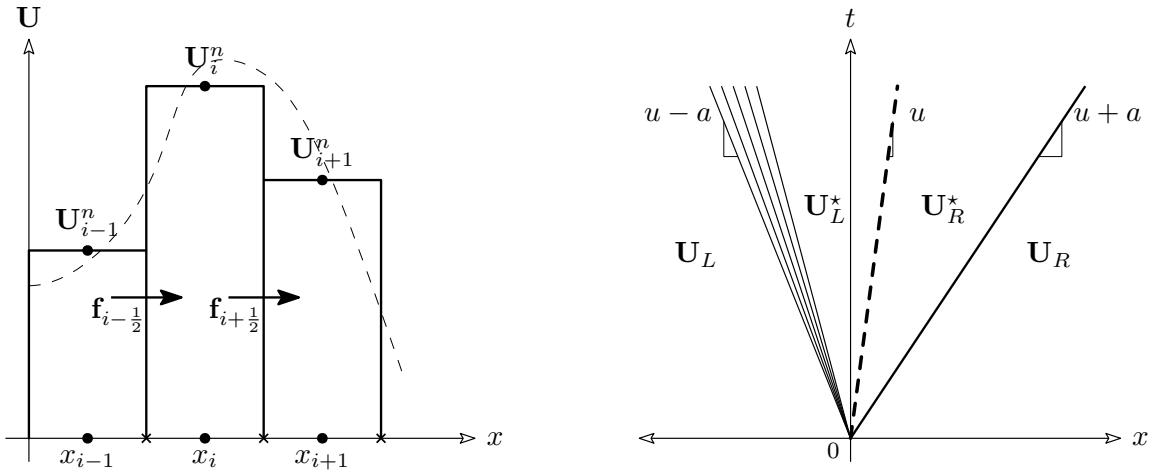

(a) Data discretisation & Riemann problem (b) Riemann solution with characteristics

Fig. 3.3 The problem discretisation onto the cell-centred points, •, shown in (a) gives rise to a Riemann problem at each cell-edged point, ×; and (b) the general Riemann solution centred about $x = 0$, with a left-moving rarefaction, central contact discontinuity, and right-moving shock.

This is the Godunov intercell numerical flux. Thus the scheme flux to step equation (3.9) forward in time is evaluated using the particular Riemann solution state vector at the cell edge.

The Riemann problem solution for the Euler equations in general has no analytic solution, but can be solved either iteratively or by approximate means. The solution consists of left- and right-travelling shock and rarefaction waves in different combinations, but always separated by a contact discontinuity. Then three characteristic waves (eigenvalues) in the solution, separate the four states shown in Figure 3.3b. The relationship between each of these states may be found using the Rankine–Hugoniot jump conditions derived from the integral form of the conservation law, and cannot be solved analytically. It should be noted that when solving a dimensionally split system, the parallel momentum equations become linearly degenerate and so the eigenvalues coincide, such that no additional characteristic waves need to be considered.

A thorough comparison of the Adaptive Noniterative approximate Riemann solver (ANRS) and Harten - Lax - van Leer Contact (HLLC) approximate Riemann solver, as well as the implementation is detailed in Wienkers (2016). However, for the following investigation the exact iterative Riemann solver as described in Toro (1999) will be used, with an initial guess provided by the ANRS. The quite popular HLLC approximate Riemann solver is not appropriate for the application presented here. This is because the “starred” pressure state approximation which the HLLC depends on for its accuracy,

suffers loss of significance at the high mach number and near-vacuum experienced near the vertical extents of the domain.

3.1.3.3 Integration

Finally, with the scheme fluxes, $\mathbf{f}$, from the spatially-discretised solution above specified as a function of the state, $\mathbf{U}$, the advection operator $\mathcal{L}_x$ and $\mathcal{L}_y$ may be found by solving the semi-discrete system of ordinary differential equations,

$$\frac{\mathrm{d}\mathbf{U}_i}{\mathrm{d}t} = -\frac{1}{\Delta x}\left(\mathbf{f}_{i+\frac{1}{2}} - \mathbf{f}_{i-\frac{1}{2}}\right) + \mathbf{S}_{\mathbf{e},i} \tag{3.23}$$

where $\mathbf{S_e}$ is the equilibrium source term responsible for the stratification. This equilibrium source term balances exactly with the discrete hydrostatic equilibrium (3.18) when solved here unsplit with the advection. Unfortunately, this prevents clever less-diffusive integration tricks from being used, such as the Hancock time-stepper (from MUSCL-Hancock), because this equilibrium source term cannot be integrated alongside the advection contribution.

A 1st order solution to (3.23) by Forward Euler gives the familiar 1D conservative update (3.9); however, an overall 2nd order scheme is desired. A good choice for a 2nd order time integration scheme which preserves the TVD properties of the spatial semi-discretisation is the 2nd order Runge-Kutta strong stability preserving (RK2SSP) scheme (Gottlieb et al., 2001),

$$\begin{aligned}
\mathbf{U}^{(1)} &= \mathbf{U}^n + \Delta t \frac{\mathrm{d}\mathbf{U}^n}{\mathrm{d}t} \\
\mathbf{U}^{(2)} &= \mathbf{U}^{(1)} + \Delta t \frac{\mathrm{d}\mathbf{U}^{(1)}}{\mathrm{d}t} \\
\mathbf{U}^{n+1} &= \frac{1}{2}\left(\mathbf{U}^n + \mathbf{U}^{(2)}\right)
\end{aligned} \tag{3.24}$$

which steps the state $\mathbf{U}^n$ forward by Δt. This integration scheme is shown to be slightly more diffusive than the MUSCL-Hancock scheme, if not only because the effective CFL number is reduced.

3.1.4 Source solver

With the advection scheme detailed above, the final solution operator of the splitting method (3.11) that is left to be found is $\mathcal{L}_s$. This source operator approximates the

solution to the initial value problem

$$\partial_t \mathbf{U} = \mathbf{S}_\mathrm{n}(\mathbf{U}, t) \tag{3.25}$$

where $\mathbf{S}_\mathrm{n}(\mathbf{U}, t)$ is the non-equilibrium-holding source terms. An adaptive step size Runge-Kutta (Fehlberg) 4^{th} order with a 5^{th} order error estimator is implemented here to solve the above differential equation while maintaining a relative error tolerance to machine precision. It should be noted that it is still necessary to solve the non-equilibrium source terms using this source splitting technique, as opposed to including it in equation (3.23) as the stable time step restriction from these source terms would detrimentally depress the CFL number.

3.1.5 Boundary conditions

The boundary conditions are enforced by introducing fictitious ghost cells around the entirety of the domain (RK2SSP requires 4 on either side). Then before each advection step, the ghost cells are updated to reflect the desired boundary conditions. This procedure is non-invasive to the the interior of the domain because each quantity is defined at cell-centre. By passively enforcing the boundary conditions in this way the finite volume method retains the desired conservative qualities.

The eccentric local model (2.19) is *not* shearing in the radial direction because the azimuthal-like velocity is actually an angular velocity. Enforcing this periodic boundary is as straightforward as updating the left ghost cells with the values from the right and similarly with the right ghost cells (except when MPI communication is required for a parallel-split domain). The domain in the periodic direction is then effectively of infinite extent and so it is apparent that this boundary is conservative.

More care must be taken to realise reflective (no-flux) vertical boundaries due to the oscillatory dynamic equilibrium. By simply using a homogeneous Neumann boundary condition on the pressure and density, the ghost cells will not be in equilibrium resulting in a continuous inward momentum flux. The density and pressure must then be extrapolated into the ghost cells by fully reconstructing the discrete equilibrium with (3.18) given the dynamic scale height, $H(t)$. Finally, the vertical velocity may be set to reflecting, as transmissive (or inflow) boundaries here can result in an ill-posed problem producing numerical instability.

3.2 Axisymmetric cartesian shearing box model

The eccentric local numerical model will similarly be constructed in light of the simpler cartesian local model presented below before continuing. A simplification over the full 3D shearing box equations (2.17) is to rather solve the axisymmetric (2.5D) system by taking every $\partial_y \to 0$. The dependence on y then drops out, and the azimuthal velocity v^y becomes a passively advected quantity in the 2.5D x-z shearing box. This allows treatment of the 3D equations which support inertial waves, while only needing to simulate two spatial dimensions. The azimuthally ($\hat{\mathbf{y}}$) invariant, conservative system, where now $\mathbf{U} = (\rho, \rho v^x, \rho v^y, \rho v^z, E)^T$ is then explicitly

$$\partial_t \begin{pmatrix} \rho \\ \rho v^x \\ \rho v^y \\ \rho v^z \\ E \end{pmatrix} + \partial_x \begin{pmatrix} \rho v^x \\ \rho v^x v^x + p \\ \rho v^x v^y \\ \rho v^x v^z \\ (E+p) v^x \end{pmatrix} + \partial_z \begin{pmatrix} \rho v^z \\ \rho v^x v^z \\ \rho v^y v^z \\ \rho v^z v^z + p \\ (E+p) v^z \end{pmatrix} = \begin{pmatrix} 0 \\ 2\rho v^y \Omega_0 + 2\rho q \Omega_0^2 x \\ -2\rho v^x \Omega_0 \\ -\rho \Omega_0^2 z \\ \rho \Omega_0^2 (2q v^x x - v^z z) \end{pmatrix}. \tag{3.26}$$

By assuming a constant background shear, $\bar{v}^y = -q\Omega_0 x$, the effective potential gradient term ($2\rho q \Omega_0^2 x$) in the $\hat{\mathbf{x}}$ momentum is balanced and cancels. Wienkers (2016) details the specific numerical implementation of this cartesian shearing box model, including various relevant validation tests.

3.3 Local eccentric model

A number of further approximations and modifications must be made to the local eccentric model (2.19) in order to implement it using the numerical methods outlined in §3.1. Nonetheless, the numerical model developed here will be presented for general thermodynamics and disc geometry (e' & ω'); however, the results will focus solely on varying the eccentricity.

3.3.1 Local axisymmetric approximation

The axisymmetric approximation will also be made in the local eccentric model (2.19) by taking each $\partial_\eta \to 0$, suppressing any non-zero azimuthal modes. This assumption is permissible because the most unstable azimuthal mode in the parametric instability is axisymmetric (Barker and Ogilvie, 2014). Unfortunately, the eccentricity looks like an $m = 1$ azimuthal inertial mode itself, so that a component of $\partial_\xi p$ still remains

in equation (2.19c) when making the axisymmetric approximation. Thus v^η is not passively advected as is the azimuthal velocity in the cylindrical model! However, by writing equation (2.19c) rather for the *covariant* velocity,

$$v_\eta = g_{\lambda\phi} v^\xi + g_{\phi\phi} v^\eta, \tag{3.27}$$

the (now angular momentum-like) equation becomes axisymmetric and can be passively advected as in §3.2. This is akin to writing the azimuthal momentum equation in terms of the specific angular momentum, which is a conserved quantity for a general eccentric disc, unlike the angular velocity. This becomes a problem only in eccentric discs due to the variation of the radial distance from the centre along an orbit. Thus the Lagrangian derivative describing the evolution of the covariant v_η is

$$Dv_\eta = \left(g_{\phi\phi}\Omega_\lambda + \Omega \left(g_{\phi\phi}\Gamma^\phi_{\lambda\phi} - g_{\lambda\lambda}\Gamma^\lambda_{\phi\phi} - g_{\lambda\phi}\Gamma^\phi_{\phi\phi} \right) \right) v^\xi + g_{\phi\phi}\Omega_\phi v^\eta, \tag{3.28}$$

which may now be advected in the Riemann solver.

A further modification to the local eccentric model of Ogilvie and Barker (2014) will also be made to help formulate a more well-posed vertical boundary, as well as permit the use of the well-balanced method. By transforming the vertical z coordinate into a coordinate system following the vertical "breathing" of the laminar solution, then the laminar oscillations become a static equilibrium. In this oscillating frame, reflective boundary conditions actually coincide with the laminar solution, and so it becomes unnecessary for "un-physical" fluid to be introduced inflowing near the boundaries just to maintain the vertical structure. The laminar solution in this formulation can also now be maintained to machine precision using the well-balanced method of §3.1.3.1.

The governing equations (2.19) are thus transformed into the oscillatory ζ coordinate, described by $z \to \zeta H(t)$. This transformation modifies the following relevant geometric terms from the definitions in the orbital coordinates of Ogilvie (2001):

$$\partial_z \to H^{-1}\partial_\zeta \tag{3.29a}$$

$$\partial_t|_z \to \partial_t|_\zeta - \frac{\dot{H}}{H}\zeta\partial_\zeta \tag{3.29b}$$

$$v^z \to H v^\zeta + \dot{H}\zeta = H v^\zeta + \bar{v}^z \tag{3.29c}$$

$$g^{\zeta\zeta} = \frac{1}{H^2} \tag{3.29d}$$

$$\Delta' = \Delta + \frac{\dot{H}}{H}. \tag{3.29e}$$

In particular, the orbital divergence term, Δ', picks up a contribution from the vertical laminar oscillations.

The governing equations (2.19) can then be rewritten in the (ξ, η, ζ) coordinates in conservation form as

$$\partial_t \begin{pmatrix} \rho \\ \rho v^\xi \\ \rho v_\eta \\ \rho v^\zeta \\ \tilde{E} \end{pmatrix} + \partial_\xi \begin{pmatrix} \rho v^\xi \\ \rho v^\xi v^\xi + g^{\lambda\lambda} p \\ \rho v^\xi v_\eta \\ \rho v^\xi v^\zeta \\ \left(\tilde{E} + p\right) v^\xi \end{pmatrix} + \partial_\zeta \begin{pmatrix} \rho v^\zeta \\ \rho v^\xi v^\zeta \\ \rho v_\eta v^\zeta \\ \rho v^\zeta v^\zeta + g^{\zeta\zeta} p \\ \left(\tilde{E} + p\right) v^\zeta \end{pmatrix} = \mathbf{S}(\mathbf{U}), \tag{3.30}$$

where the source term on the right side is

$$\mathbf{S}(\mathbf{U}) = \begin{pmatrix} -\rho\Delta' \\ -\rho v^\xi \Delta' - 2\rho\Omega \left(\Gamma^\lambda_{\lambda\phi} v^\xi + \Gamma^\lambda_{\phi\phi} v^\eta\right) \\ -\rho v_\eta \left(\Delta' + \Omega_\phi\right) + \rho v^\xi \left(g_{\lambda\phi}\Omega_\phi - g_{\phi\phi}\Omega_\lambda + \left(g_{\lambda\lambda}\Gamma^\lambda_{\phi\phi} + g_{\lambda\phi}\Gamma^\phi_{\phi\phi} - g_{\phi\phi}\Gamma^\phi_{\lambda\phi}\right)\Omega\right) \\ -\rho v^\zeta \Delta' - \rho\Phi_2\zeta - 2\rho v^\zeta \frac{\dot{H}}{H} - \rho\frac{\ddot{H}}{H}\zeta \\ -\left(\tilde{E} + p\right)\Delta' - \rho\Omega v_\eta \left(v^\xi \Gamma^\phi_{\lambda\phi} + v^\eta \Gamma^\phi_{\phi\phi}\right) + \rho\Phi_2 H^2 \left(\frac{1}{2}\zeta^2\Delta - \zeta v^\zeta\right) - \rho v^\zeta H \left(\dot{H} v^\zeta + \ddot{H}\zeta\right) \end{pmatrix} \tag{3.31}$$

The perturbation energy, $\tilde{E}$, is also redefined as

$$\tilde{E} = e + {}^1\!/_2\rho \left(g_{\lambda\lambda} v^\xi v^\xi + 2 g_{\lambda\phi} v^\xi v^\eta + g_{\phi\phi} v^\eta v^\eta + g_{\zeta\zeta} v^\zeta v^\zeta\right), \tag{3.32}$$

which must be used to cancel out the additional vertical pressure gradient term in the energy equation.

3.3.2 Modified Riemann problem and finite volume scheme

The $g^{\lambda\lambda}$ and $g^{\zeta\zeta}$ inverse metric terms that arise in the ξ and ζ flux now imply that the finite volume advection is anisotropic. This necessitates a number of modifications to the Riemann solver as well as the finite volume scheme. As these metric terms vary with time, the ξ and ζ coordinates stretch and contract periodically around the disc. Thus the characteristics in an inertial cartesian system where the Riemann problem is posed are curved, which requires consideration of the generalised Riemann problem. Nonetheless, for a first approximation, the geometric coefficients may be held constant for the short duration of each advection time step. Convergence can then be shown as $\Delta t \to 0$, as the quasi-constant characteristics better represent the true

curved characteristics. In this approximation, the standard Riemann problem (3.21) is transformed by simply scaling the characteristics by $\sqrt{g^{\lambda\lambda}}$ and $\sqrt{g^{\zeta\zeta}}$ when solving in the split ξ and ζ direction, respectively.

From the local expansion in §2.2.2, each of the geometric terms are evaluated on the reference orbit, $(\lambda_0, \varphi(t), 0)$, and so are implicit functions of time only. The orbital location of the local coordinates, $\varphi(t)$, must then be determined as a function of time. This requires solving the ODE

$$\frac{\mathrm{d}\varphi}{\mathrm{d}t} = \Omega(\lambda_0, \varphi) = \sqrt{\frac{GM}{\lambda_0^3}} \left(1 + e\cos\theta\right)^2 . \tag{3.33}$$

Alternatively, a more accurate solution may be obtained by using Kepler's method to determine the true anomaly as a function of time. This is found by directly computing

$$\theta(t) = 2\tan^{-1}\left(\sqrt{\frac{1+e}{1-e}}\tan\left(\frac{\mathcal{E}}{2}\right)\right) \tag{3.34}$$

where the eccentric anomaly, $\mathcal{E}$, is first found by numerically solving

$$\frac{2\pi t}{\mathcal{P}} \bmod 2\pi = \mathcal{E} - e\sin\mathcal{E} \tag{3.35}$$

for example by using the Newton-Raphson method. Thus $\varphi(t) = \theta + \omega$ can be quickly computed at each time step. The transformation into ζ coordinates also requires the horizontally invariant laminar solution describing $H(t)$ to be found at each time step. For efficiency, $H(t)$ is calculated once at the start of each simulation, and then these tabulated values used around each orbit.

Two additional source terms arise in the ζ-momentum equation as a result of the transformation into vertically oscillating coordinates. The first comes from the flux of ζ-momentum by the grid velocity, whereas the second term arises from the acceleration of the grid. This $-\rho\ddot{H}/H\zeta$ term may be interpreted as coming from an additional potential, $\ddot{H}/H$, and which must be included into Φ in the well-balanced correction (3.19) to maintain this "static" equilibrium. The equilibrium source term to be solved unsplit in the ζ-momentum component of (3.23) is then

$$S_\mathrm{e} = -\rho\left(\Phi_2 + \frac{\ddot{H}}{H}\right). \tag{3.36}$$

3.3.3 Problem setup

The numerical implementation of the methods described above, as well as the following results are given in units of length such that the circular disc isothermal scale height, H_0, is unity. The unit of time is also defined such that the angular velocity, Ω_0 at $r = \lambda_0$ is unity, so that the linear velocities are nondimensionalised by the isothermal sound speed. Finally, the mid-plane density at apocentre is set to be 1.

The standard numerical problem setup that was used for each of the base runs evolves an initial perturbation on a centred domain with height $L_\zeta = 12$, and width L_ξ chosen to exactly fit the wavelength of the perturbation, $2\pi/k_\xi$. Although tests included the $n = 1, 2, 3$ modes, the following will focus on the $n = 1$ vertical mode, where the $\omega = 1/2$ perturbation has radial wavenumber $k_\xi = 3/2$. For this mode, the vast majority of the perturbation energy is represented in the domain, with less than 10^{-7} of the total energy not captured in the first 6 scale heights (see Figure 2.6).

The Minbee limiter was chosen for these standard runs, because although more numerically diffusive, is necessary for stability near the boundary for larger eccentricities. To that end, the last two scale heights were also reduced to a 1^{st} order spatial reconstruction.

A standard resolution of $N_\xi = 128$ was used, with N_ζ chosen so that $\Delta\xi = \Delta\zeta$ to minimise any anisotropic numerical diffusion that could cause spurious results. For $n = 1$ then, $N_\zeta = 366$. With this resolution, a typical evolution time of 1000 orbital periods requires around 500 CPU-hours.

The domain is initialised with the discrete isothermal density profile (3.18) and the equilibrium velocities equal to naught. An exact inertial wave perturbation is added, producing a standing wave with $|v^\xi| = 10^{-3}$. The form of this perturbation is

$$\begin{pmatrix} h' \\ v^\xi \\ v^\eta \\ v^\zeta \end{pmatrix} = \begin{pmatrix} -k_\xi\omega^2 \\ \omega(\omega^2 - n) \\ \frac{1}{2}(\omega^2 - n) \\ nk_\xi\omega/H \end{pmatrix} \cdot \begin{pmatrix} \sin(\omega t + \pi/4) & \sin(k_\xi\xi - \pi/4) \\ \sin(\omega t - \pi/4) & \sin(k_\xi\xi + \pi/4) \\ \sin(\omega t + \pi/4) & \sin(k_\xi\xi + \pi/4) \\ \sin(\omega t - \pi/4) & \sin(k_\xi\xi - \pi/4) \end{pmatrix} \tag{3.37}$$

which has a vertical structure given by (2.37).

3.3.4 Model verification

The 1D Toro (1999) validation tests are presented in Appendix B for the above described finite volume implementation using the TVD RK2SSP integrator with the Minbee limiter and exact Riemann solver as it is implemented for the standard

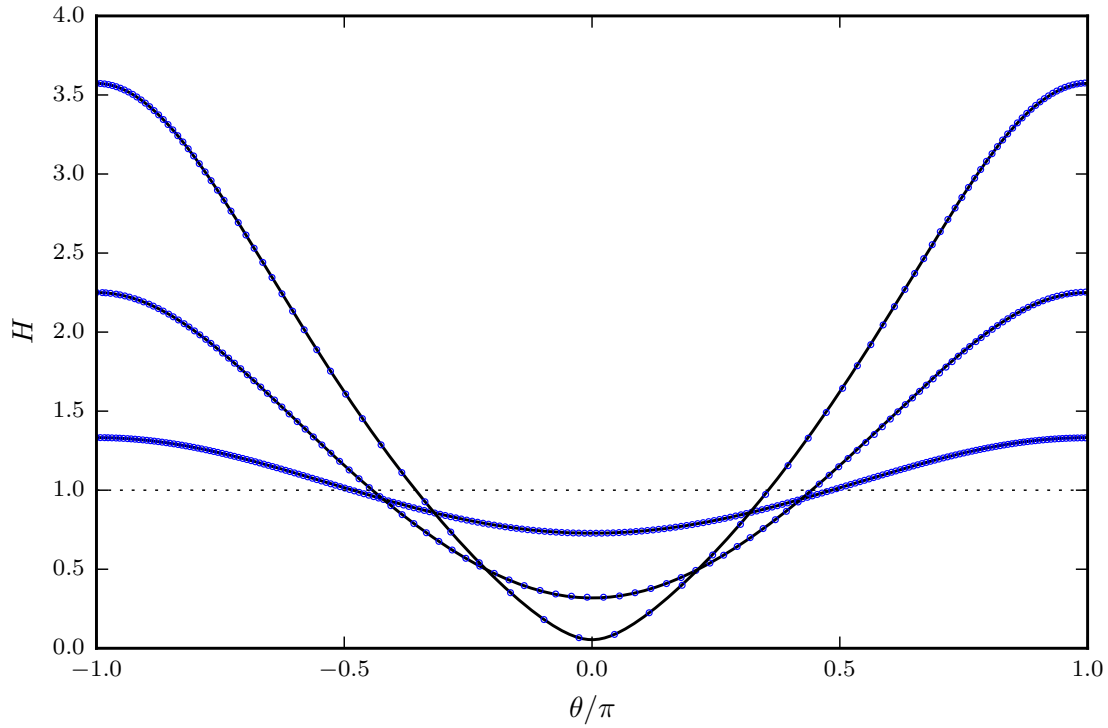

Fig. 3.4 The scale height evolution shown here over one orbit computed in the z coordinate system using the well-balanced scheme and $H_{\rm peri}/\Delta z = 6.0$ for $e = 0.1$, 0.3, and 0.5. Each semi-analytic solution is given for reference.

runs. As expected, compared with the often-used MUSCL-Hancock scheme, the RK2SSP integrator is found to be slightly more dissipative, smearing out strong shocks particularly in test 1 shown in Figure B.1.

3.3.4.1 Horizontally invariant laminar solutions

The described implementation (§3.1) is first tested in the untransformed z coordinates to ensure agreement with the semi-analytic horizontally invariant laminar solution given by (2.27). The results over a single orbit for $e = 0.1$, 0.3, and 0.5 show good agreement with the analytic solution (see Figure 3.4); however, for longer evolution times with moderate eccentricities, the vertical boundaries were found to produce errors by slowly degrading the similarity solution profiles (2.24). The no-flux boundary produces a weak rarefaction wave which eventually affects the midplane. Unfortunately, a transmissive reconstructive boundary still creates an ill-posed problem due to the fluid inflow. Hence, the oscillatory vertical geometry (ζ) is adopted, and will now be tested.

3.3.4.2 Well-balanced ζ equilibrium

It is first critical that this new implementation, in particular due to the modified splitting method, produces the correct physical frequencies in response to specific perturbations. Thus the initial conditions described in §3.3.3 with $e = 0$ and $n = 0, 1, 2$ are evolved for 1000 orbital periods to gain high frequency resolution. The response is subsequently Fourier analysed to extract the relevant frequencies, and which are found to agree with those given by the dispersion relation down to the frequency resolution.

Throughout the course of these long runs the amplitude of the initial perturbation inevitably decreases. Although no explicit viscosity is prescribed, momentum diffusion across cell boundaries inherent to discretisation is unavoidable, and produces an effective numerical viscosity. This effective α-viscosity due to numerical dissipation may be measured given the properties of the test perturbation and the decay rate by

$$\alpha \sim \frac{\sigma_{\text{damp}}}{k_\xi^2 + n}. \tag{3.38}$$

For a typical run with $k_\xi = 3/2$ and $n = 1$, the perturbation decays to nearly 50% of the initial amplitude over the course of 1000 periods, corresponding to a damping rate of $\approx 10^{-4}$. The effective numerical α-viscosity is then approximately $\alpha_{\text{n}} \approx 3 \cdot 10^{-5}$. Although this exceeds the molecular viscosity $\alpha \approx 10^{-9}$, it is still orders of magnitude smaller than the expected and observed values of α, as well as more than 100 times less diffusive than comparable global simulations with vertical structure (Bitsch et al., 2013). This numerical viscosity may also be halved by doubling the resolution, as well as by not using a slope limiter, but at the expense of less numerical stability.

The linear growth rate of these simulations can then be shown to agree with the $\sigma = {}^3\!/_4 e$ from linear theory, less this numerical damping rate.

3.3.4.3 Well-balanced convergence study

The 2$^{\text{nd}}$ order RK2SSP well-balanced implementation is now compared against the standard unbalanced MUSCL-Hancock scheme in a convergence study of the deviation from the laminar solutions. The discrete hydrostatic equilibrium with no initial velocity perturbation is evolved for 10 periods in a disc with $e = 0.1$ so as to also demonstrate the consistency of the quasi-constant geometry approximation of §3.3.2. As evidenced in Figure 3.5, the well-balanced scheme nearly maintains the laminar oscillations to machine precision. Near the mid-plane, however, it maintains the equilibrium exactly

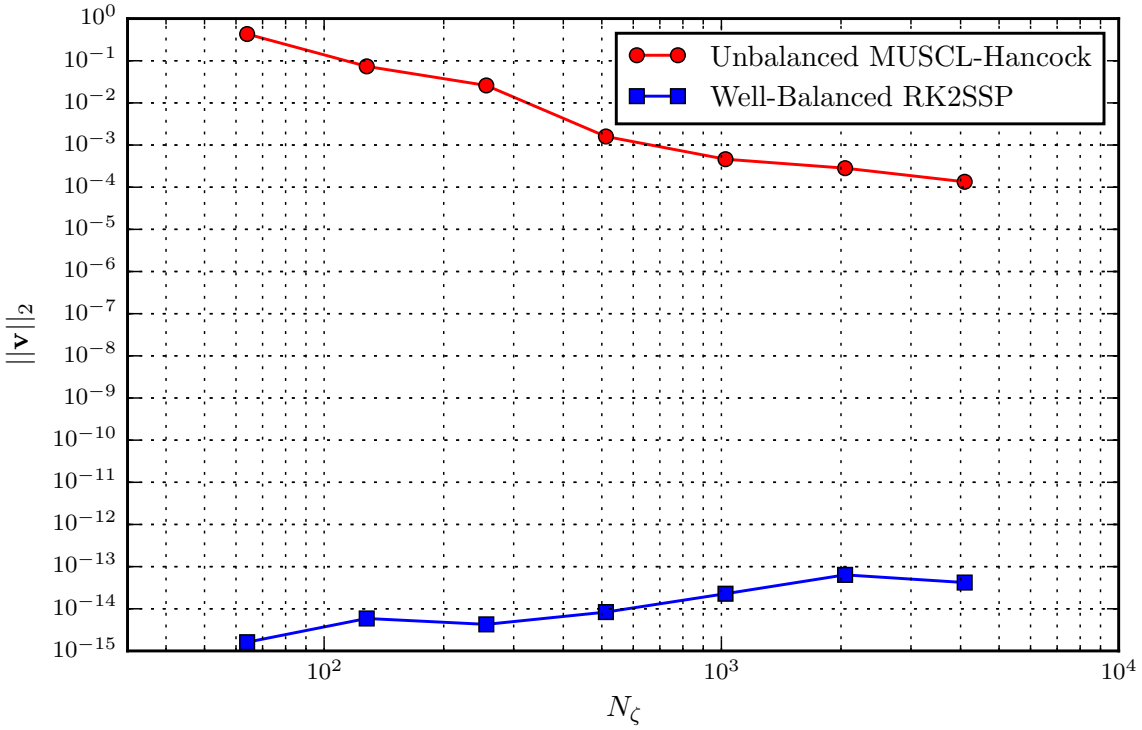

Fig. 3.5 L_2-norm error of the velocity for the well-balanced and unbalanced schemes, in a test to hold the "static" laminar solution.

to machine precision, whereas near the boundaries, the machine precision perturbations from the midplane amplify as they travel into the increasingly rarefied atmosphere.

This is compared to the unbalanced MUSCL-Hancock scheme, in which errors arise due to the operationally-split nature of the algorithm trying to balance the pressure gradient independently from the gravitational source. Thus without the well-balanced method, a prohibitive 10^8 grid points would be required with this 2^{nd} order source-split scheme!

Chapter 4

Results and Discussion

The well-balanced finite volume method evolving the local eccentric axisymmetric model as described previously has been implemented and will now be employed to study the nonlinear effects which are initially produced by the breaking of inertial waves.

4.1 Development of breaking inertial waves

The evolution of each numerical simulation is initialised with a perturbation of amplitude $\sim 10^{-3}$, which is well within the linear parametric growth phase. However, this linear instability soon gives way to a saturated growth rate as the linear theory begins to break down. This is initially due to the breaking of inertial waves, but when fully developed may include more complex wave-wave interactions. In an unrestricted domain, due to the monotonic ($n = 1$) vertical profile, there always exists a height above the midplane with a large enough amplitude to feel these nonlinear effects, however small the energy contribution. In a limited computational domain, only eventually will the waves begin to break at the vertical extents, first appearing as a local increase in the azimuthal shear. The criterion for breaking from §2.3.3 written as $k_\xi \delta\xi \approx 1$ implies there is a local increased convergence from the fluid over-extension in $\hat{\xi}$, consequently producing a vertical jet. This initial breaking process is demonstrated in Figure 4.1, showing three snapshots at apocentre, taken at $\tau = 44$, 52, and 60, where $\tau = t/\mathcal{P}$. Each of the columns from left to right give contours of v^ξ, v^η, and v^ζ respectively.

The critical v^ξ motivated in §2.3.3 can also be roughly verified on these plots. Although it is not clear exactly when an inertial wave is considered broken, shortly after the snapshot at $\tau = 44$, $v^\xi \approx 0.33$ is observed as predicted. One apparent effect of inertial wave breaking is that the phase of the in-plane velocity perturbations

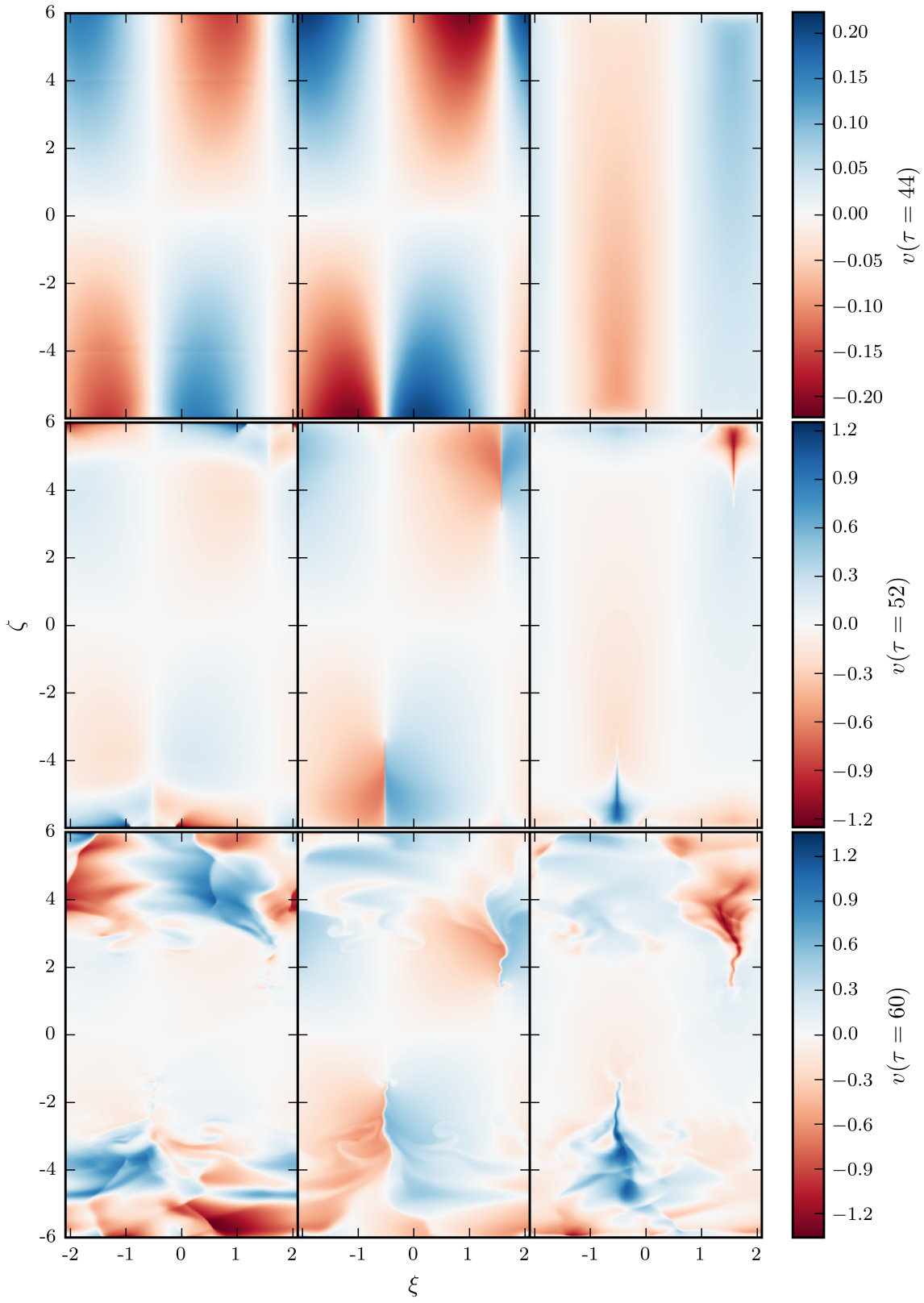

Fig. 4.1 The initial inertial wave breaking period shown for a disc with $e = 0.02$. Velocity snapshots shown (from top to bottom) just before ($\tau = 44$), during ($\tau = 52$), and shortly after ($\tau = 60$) the initial wave breaking. The velocities from left to right are v^{ξ}, v^{η}, and v^{ζ}.

abruptly shifts, lagging by more than $\pi/2$ compared to in the linear growth regime (cf. v^ξ at $\tau = 52$ in Figure 4.1). This point will become more important when discussing the evolution of α.

4.2 Saturation of the parametric instability

After this initial ordered wave breaking period which causes a slight overshoot in the perturbation energy, the mode is finally recovered before the secondary instability saturates the temporal evolution into a steady turbulent state. This steady turbulence is characterised by subsonic fluctuations with a typical root-mean-square vertical velocity of $v^z_{RMS} \approx 0.4$, except at large distances from the mid-plane for moderate eccentricity where the fluctuations are marginally supersonic. This dependence on eccentricity is shown in Figure 4.2 and may be compared to the typical velocities an order of magnitude smaller that were found in the numerical simulations by Papaloizou (2005a) in a disc without vertical structure. His global disc simulations with $e \approx 0.13$ produced typical $v^z_{RMS} \approx 0.03 c_s$ constant over the height of the disc.

4.2.1 Heuristic model for energy transport in a stratified disc

A heuristic model may be constructed by using turbulent kinetic energy transfer and localisation arguments to gain insight into the energy saturation behaviour in Figure 4.3. Saturation of the parametric (primary) instability is caused by the dissipation of the parametrically excited mode by a secondary instability, which includes inertial wave breaking as well as other wave-wave interactions. Further insight may be had into the perturbation energy transfer by considering local energy balances at each height. This will then be extended by making a global energy balance between the primary instability sourcing energy and decay from the secondary instability, allowing a scaling of the energy saturation point to be deduced.

Assuming that the perturbation energy is localised to particular ζ by the disc stratification, the specific turbulent kinetic energy contained in wavenumber k, at height ζ, may be written as $\varepsilon(k,\zeta) = {}^1\!/_2 \langle g_{ij} v^i v^j \rangle$. The evolution of this turbulent kinetic energy is then locally described by

$$\partial_t \varepsilon(k,\zeta) = T(\varepsilon,k) + G(\varepsilon,k) + F(k,\zeta) - 2\nu k^2 \varepsilon(k,\zeta), \tag{4.1}$$

for each k and ζ, although fluctuations at different heights may interact via the energy flux term, $F(k,\zeta)$, and different wavenumber fluctuations can communicate through

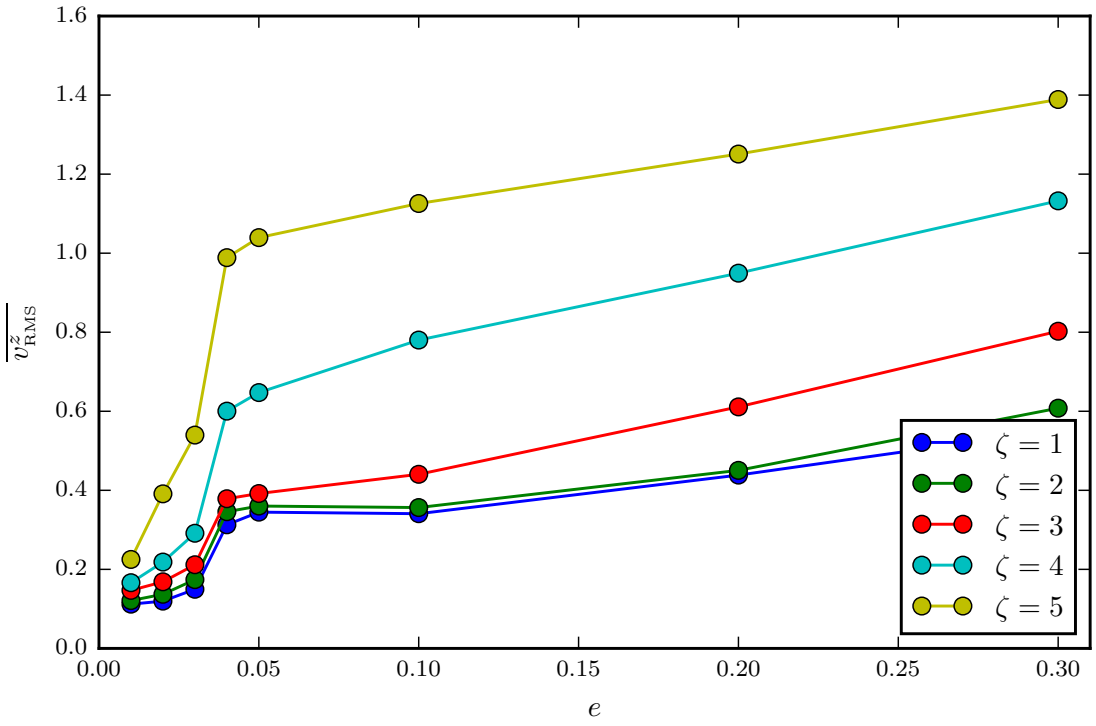

Fig. 4.2 The vertical RMS velocity is shown at various heights scaling with the eccentricity. The majority of the fluid remains subsonic, though with large enough forcing the vertical extents of the disc become supersonic.

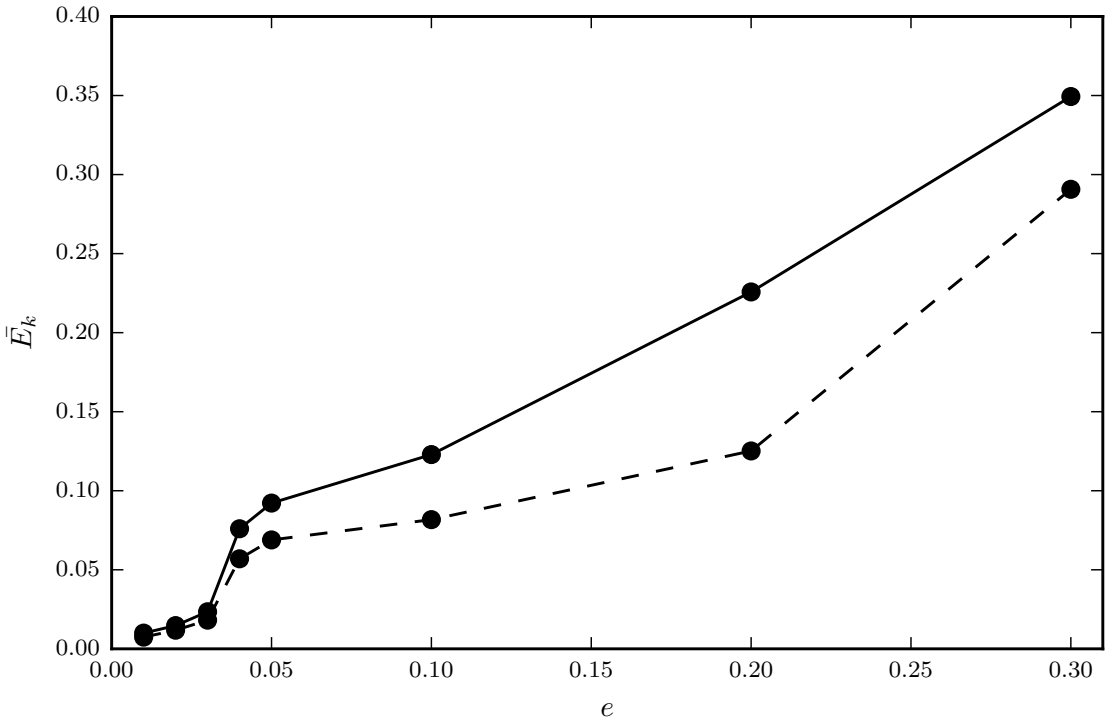

Fig. 4.3 The total kinetic energy (solid line) and kinetic energy in the parametrically excited mode (dotted line) at saturation are shown scaling with the eccentricity. For small eccentricity, the majority of the energy remains in the initial mode.

the triadic term, $T(\varepsilon, k)$. These triadic interactions describe the cascade of energy to higher wavenumbers due to the transport and stretching of the perturbations by the nonlinear advection term in the Euler equations and so are not localised in k-space. Finally, the linear growth rate of the parametric instability increases only the energy of the parametrically excited wavenumber, k_0, as $G(\varepsilon, k) = {}^3\!/_4 e\Omega\varepsilon \cdot \delta(k - k_0)$ where δ here is the Kronecker delta function. Although there is no explicit dissipation prescribed in the numerical model, the dissipation rate at the smallest length scales are still described by a molecular (or numerical) viscosity, ν.

This model will now be analysed at the steady turbulent state, where $\partial_t \varepsilon = 0$ for each k and ζ, by first focussing on the perturbations at $\zeta = \zeta_{\text{crit}}$, where the inertial waves begin to break and dissipate energy. For $k = k_0$ at this height, there is very little dissipation because k_0 is small. Thus the energy flux from $\zeta < \zeta_{\text{crit}}$ along with the instability energy growth are balanced by transferring the energy to smaller scales (k') via triad interactions:

$$F(\zeta < \zeta_{\text{crit}}) + G(k_0) \longrightarrow T(k' > k_0). \tag{4.2}$$

However, considering now $k > k_0$, at ζ_{crit}, there is no parametric growth term, and so energy at k' is solely transferred through k to smaller scales and dissipated:

$$T(k' < k) \longrightarrow T(k' > k) + 2\nu k^2 \varepsilon(k). \tag{4.3}$$

Physically, the energy here proceeds to cascade to smaller scales, down to the order of the mean free path where molecular viscosity is able to dissipate it as heat; however, numerically this turbulent cascade is preempted by the grid size. Nonetheless, the energy is similarly "dissipated" by the energy conservation scheme when the momentum is no longer able to be represented on the subgrid-scale.

Now considering the remainder of the disc, at $\zeta < \zeta_{\text{crit}}$, it is reasonable to say that $T(\zeta) \ll T(\zeta_{\text{crit}})$ for all k (i.e. the perturbations are very weakly nonlinear). Additionally, because the majority of energy remains in the k_0 mode, little dissipation occurs, so that the perturbation energy is only diffused across ζ:

$$G(k) + F(\zeta) \longrightarrow F(\zeta' \lessgtr \zeta). \tag{4.4}$$

Due to the vertical flux conservation for $\zeta < \zeta_{\text{crit}}$, all energy is eventually transported through ζ_{crit} at k_0. At these large scales, the energy must go through the triadic term at k_0 (4.2), and so the turbulent cascade may be parameterised by an eddy viscosity,

ν_T, above ζ_{crit}, which accounts for the energy dissipation at $k > k_0$. Thus $\nu_T k_0^2 \varepsilon$ takes the place of T above ζ_{crit}, permitting a macroscopic and global energy balance.

Energy is injected by the disc eccentricity at a given k_0 for all ζ, written as

$$\partial_t \tilde{E}_{k,\text{gain}} \approx \int_0^\infty \frac{3}{4} e\Omega\rho\varepsilon_0 \,\mathrm{d}\zeta \sim \tilde{E}_k e\Omega, \tag{4.5}$$

where $\tilde{E}_k$ is the total perturbation kinetic energy. The approximation $\tilde{E}_0 \approx \tilde{E}_k$ has been used here, which is seen to be true for small eccentricity (cf. Figure 4.3). This total energy growth is balanced with the dissipation by the parameterised turbulent viscosity term above ζ_{crit}:

$$\partial_t \tilde{E}_{k,\text{loss}} \approx \int_{\zeta_{\text{crit}}}^\infty \rho\nu_T k_0^2 \varepsilon \,\mathrm{d}\zeta. \tag{4.6}$$

A scaling for this turbulent viscosity motivated by the mixing length model for large eddy transport suggests $\nu_T \propto \sqrt{\varepsilon}/k_0$. Additionally, a linear velocity profile ($n = 1$) is assumed for all ζ, so that

$$\varepsilon = \frac{\varepsilon_{\text{crit}}}{\zeta_{\text{crit}}^2} \zeta^2, \tag{4.7}$$

allowing the scaling of integral (4.6) to be found. A similar analysis may also be done for the other inertial modes using profiles of higher powers in ζ, with conceptually similar results.

Balancing these two energy integrals finally gives a scaling for the total energy at saturation,

$$\tilde{E}_k \approx \frac{a}{e} \frac{2 + \zeta_{\text{crit}}^2}{\zeta_{\text{crit}}^3} \mathrm{e}^{-\zeta_{\text{crit}}^2/2} \tag{4.8}$$

for some proportionality constant a. To find closure, the final conservation argument relating the total energy to ζ_{crit} is

$$\begin{aligned} \tilde{E}_k &= \int_0^\infty \rho\varepsilon \,\mathrm{d}\zeta && (4.9)\\ &\approx \frac{\varepsilon_{\text{crit}}}{\zeta_{\text{crit}}^2} \int_0^\infty \rho\zeta^2 \,\mathrm{d}\zeta && (4.10)\\ &\approx \frac{b}{\zeta_{\text{crit}}^2}. && (4.11) \end{aligned}$$

where it was assumed that $\varepsilon_{\text{crit}} \propto v_{\text{crit}}^2 \propto 1$ as suggested by §2.3.3. The magnitude of the proportionality constant b is then expected to be $b \sim 3\rho_0 v_{\text{crit}}^2$. The total energy

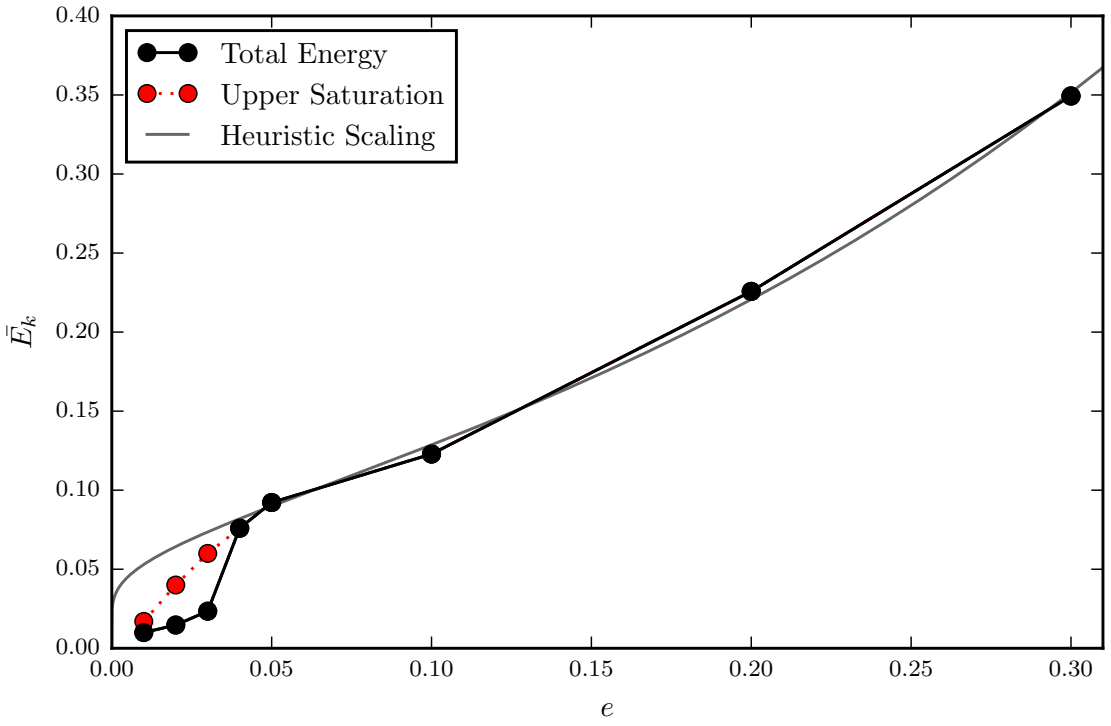

Fig. 4.4 The total kinetic energy at saturation is shown with the best fit function (4.12). The upper saturation energy level is also shown when it significantly differs from the average at small eccentricities as seen in Figure 4.5.

can then be implicitly represented in terms of the eccentricity as

$$\frac{a^2\left(b+2\tilde{E}_k\right)^2}{b^3\tilde{E}_k}\mathrm{e}^{-b/\tilde{E}_k} \approx e^2, \tag{4.12}$$

which may be solved numerically for $\tilde{E}_k$.

The best fit function of the form (4.12) was found for the constants $a = 0.089$ and $b = 0.452$, and is plotted over the saturation energy scaling in Figure 4.4. As will be considered in the following section, at small eccentricities a low frequency weakly nonlinear oscillation may occur in which the saturation point flips between a high and low energy state. In particular, for $e = 0.02$ and 0.03, the averaged energy differs significantly from this upper saturation level, and as shown in Figure 4.4, appears to better match the form of this heuristic model. Still, the assumptions made to formulate this model are unable to explain the sensitive threshold point for the weakly nonlinear oscillations, yet the model fits the scaling quite well in the more strongly nonlinear

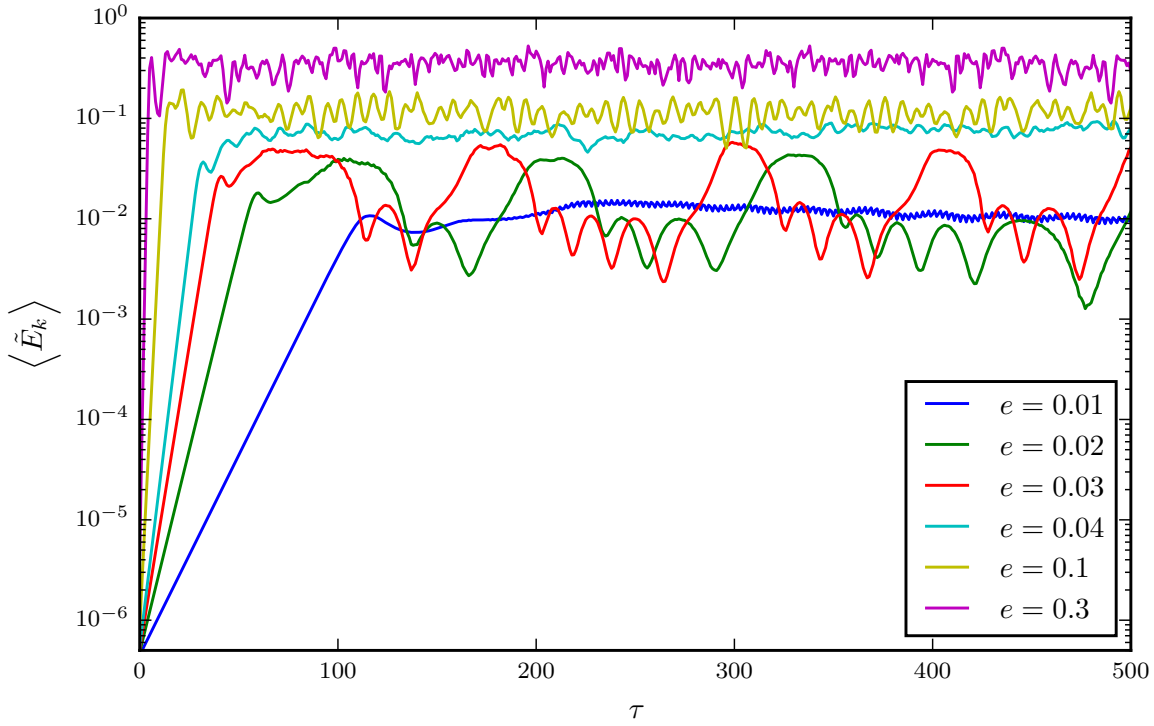

Fig. 4.5 Comparison of the long-time saturation behaviour with increasing eccentricity. Low frequency weakly nonlinear oscillations in the saturation energy are evident in particular for $e = 0.02$ & 0.03.

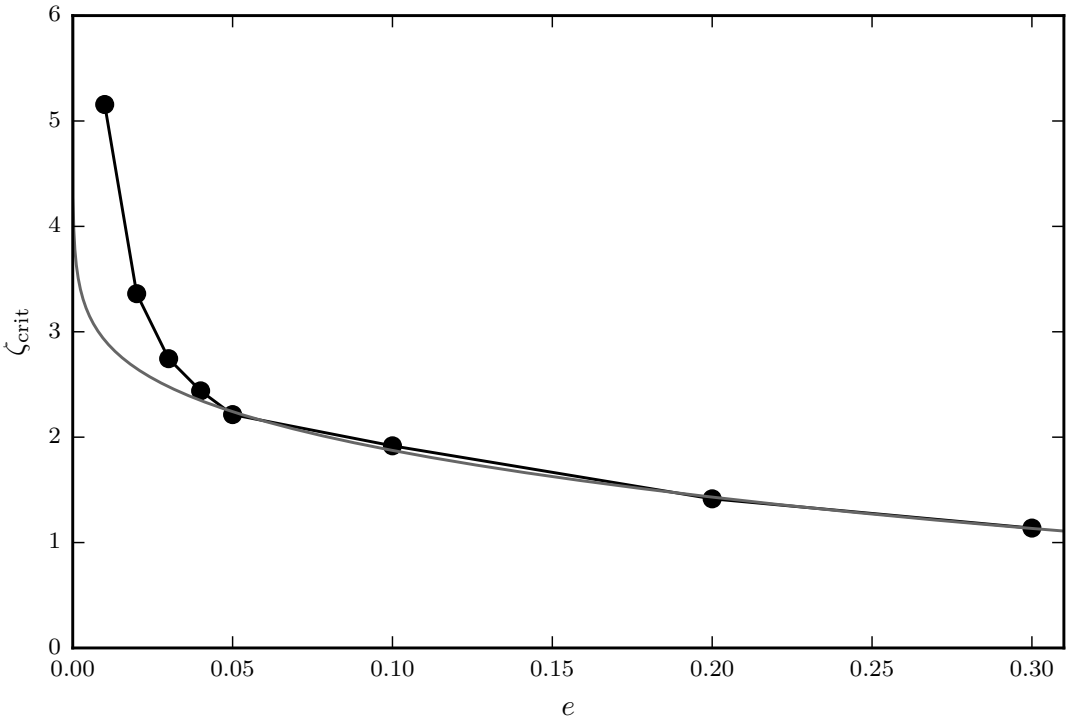

Fig. 4.6 The predicted saturation height above the disc midplane for the heuristic model compared to in simulations, assuming $v_{\rm crit}$ is constant.

regime. Further, the value of b implies that $\varepsilon_{\rm crit} \sim 0.38$, or that $v^{\xi}_{\rm crit} \sim 0.35$. This critical value for v^{ξ} is only slightly larger than the value of 0.33 estimated in §2.3.3, but could be expected as the argument presented there was only indicating the point of initial breaking.

The estimated values for $\zeta_{\rm crit}$ from this model are compared to those found in simulations and shown in Figure 4.6. As expected, as more energy is required to be dissipated (with increasing eccentricity), then $\zeta_{\rm crit}$ must encroach on the higher densities near the midplane. Thus, only localised parts of the disc both become unstable to the secondary instability *and* are able to dissipate sufficient energy. Below $\zeta_{\rm crit}$, the inertial waves are not significantly nonlinear, whereas above $\zeta_{\rm crit}$ the perturbation energy available to dissipate decreases in the more rarefied atmosphere. It may then be expected that $\zeta_{\rm crit}$ remains further from the midplane for higher inertial modes because the perturbation energy profile extends higher (as in Figure 2.6). Nonetheless, as it was shown that $v_{\rm crit}$ is nearly constant, the most kinetic energy is available to the $n = 1$ mode because this profile is contained nearest the midplane. This particular behaviour is a consequence of the vertical disc structure, and so is unique to stratified atmospheres.

4.2.2 Self-regulation

As noticed in the previous section, when the secondary instability saturating growth is only weakly nonlinear, oscillations at saturation may be produced due to the modulation of the linear terms by weakly nonlinear effects. These oscillations are most pronounced for $e = 0.02$ and 0.03, as evident in Figure 4.5. The timescale of these oscillations is found to decrease with increasing eccentricity. Very long timescale undulations exist at saturation for $e = 0.01$, compared to the strongly nonlinear saturation at higher energy where eventually there is no obvious separation of timescales. At the threshold near $e = 0.02$, the energy is found to reside in two distinct energy states, the lower of which has an average energy even below the saturation level for $e = 0.01$. The presence of these oscillations is found to be quite robust; however, their quality is extremely sensitive to the numerical dissipation as well as any initial noise. For example, the exact residence time in the high compared to the low energy states may change, although the particular saturation levels are not affected.

These oscillations may also be seen as a self-regulation process at saturation. As the secondary instability depletes the primary mode of too much energy, the inertial waves no longer break. The primary signal subsequently regains a near-linear growth rate until eventually overshooting $v^{\xi}_{\rm crit}$ producing further unbalanced dissipation as

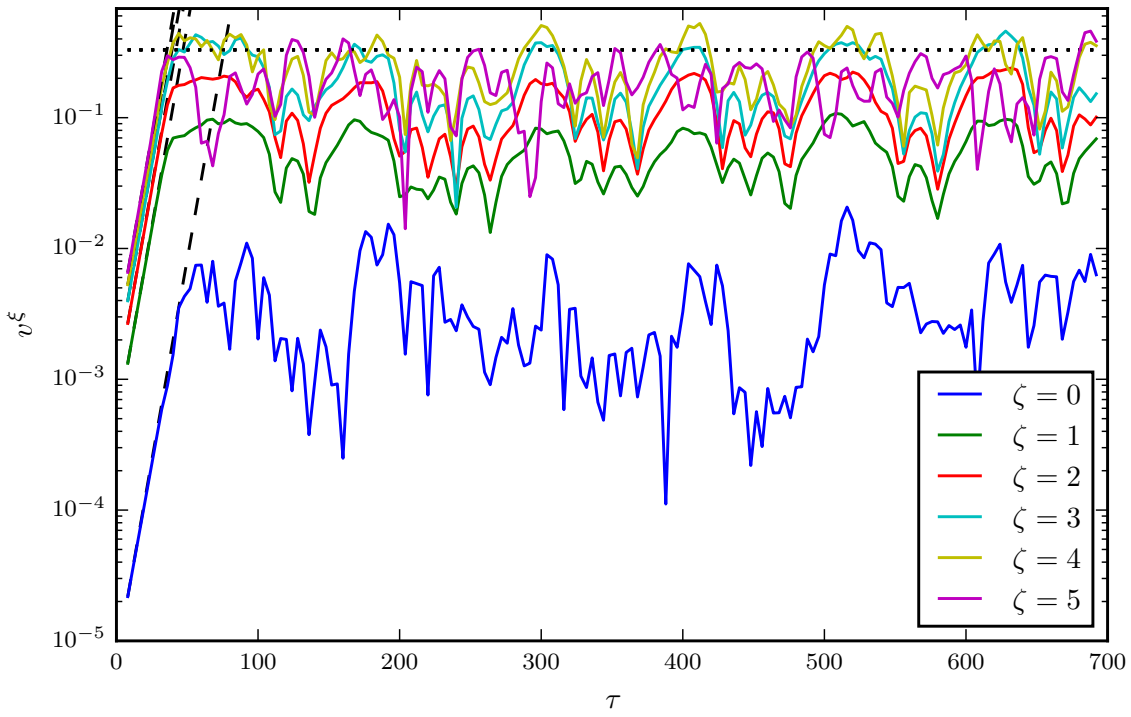

Fig. 4.7 The velocity of the parametrically unstable ($\omega = 1/2$) mode is shown at various heights in the disc with $e = 0.03$. v^{ξ} is seen to oscillate around the critical inertial wave breaking amplitude, v^{ξ}_{crit} (dotted line).

evidenced in Figure 4.7. Thus it makes sense that the modulation frequency increases with the "stiffness" of the system, being the linear growth rate.

Beyond this weakly nonlinear saturation regime for $e \lesssim 0.03$, the saturation energy is pushed into a more strongly nonlinear regime, which appears as the large jump at $e = 0.04$ in the saturation energy scaling (Figure 4.4).

4.2.3 Convergence study

Chaotic behaviour is common for nonlinear dynamical systems, such as this inertial wave breaking and interaction process. This causes extreme sensitivity to the initial conditions as well as any inevitable numerical dissipation. Nonetheless, the energy saturation level was confirmed to be statistically independent of the particular initial conditions and resolution used in the evolution through an extensive convergence study targeting $e = 0.02$ and $e = 0.1$. In particular, when initialised with a random velocity field, the resonant mode is selected, and consistently saturates. Nonetheless, there is still an unavoidable bias due to the size of L_{ξ}, as this will preferentially choose the

mode supported in an integer size of the domain. Therefore, it was also shown that these results are independent of the box size by using a domain twice the size for the $n = 1$ mode. This domain size also nearly supports the $n = 2$ mode, yet little change was noticed due to sharing the energy between modes.

Finally, convergence with resolution (or more generally with decreasing numerical dissipation) was shown for the energy saturation level. However, values based on the Reynolds stresses are notoriously difficult to converge without sub-grid turbulence models or direct numerical simulations. This is because although often insignificant to the larger scales (given no backscatter interaction), sub-grid scale fluctuations still contribute to the Reynolds stresses, and therefore α and the eccentricity decay rate. This means that the value calculated for α will always depend on the grid size (King et al., 2007)! Thus as expected, with 4 times higher resolution, the magnitudes computed for the Reynolds stresses consistently increase by around 20%.

4.3 Angular momentum transport

The integral (2.32) around the disc is computed discretely within the code after each time step to determine the efficiency with which this turbulent state transports angular momentum. A typical time evolution of α is shown in Figure 4.8, where three distinct phases are noted. In the initial linear growth phase, $\alpha \approx 0$ as Reynolds shear stresses in the plane of the disc nearly cancel out over the course of a perturbation period ($2\mathcal{P}$). Due to the linear growth rate breaking the symmetry of the integral, α is very slightly negative. This can be shown using equation (2.32), with the eigenvector (3.37) and growth rate $\exp(\gamma t)$.

As the inertial waves grow, $-\alpha$ increases exponentially until beginning to feel the nonlinear effects of wave breaking. Coincident with this decrease in α, the phase of both v^ξ and v^η shift, lagging by nearly 120 degrees. Although they similarly lag, their phase separation increases slightly from $\pi/2$, causing a negative velocity correlation which also contributes to the dip in α seen in Figure 4.8 after $\tau = 100$. This phase shift is more pronounced further from the midplane where the waves first break, and so initially does not contribute significantly to the angular momentum transport.

Once the disc has reached a steady turbulent state, large amplitude fluctuations in α are produced which average out to be small and negative. This averaged value of α is shown scaling with eccentricity in Figure 4.9. A sharp transition between $e = 0.03$ and $e = 0.04$ is again associated with the secondary instability being pushed away from the weakly nonlinear regime. Additionally, for large eccentricity, the $g^{\lambda\phi}p$ term in the

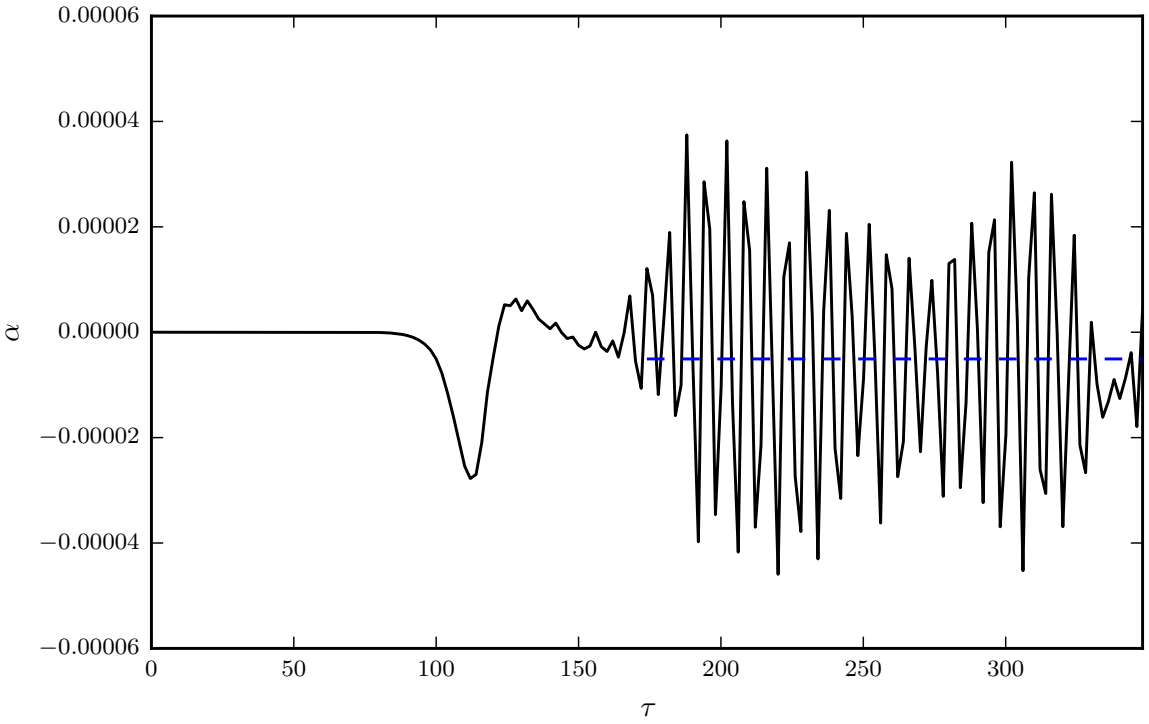

Fig. 4.8 The α-viscosity evolution for $e = 0.01$, showing the integrated value over $2\mathcal{P}$. The large scale oscillations present after saturation average to a small but negative value (blue dotted line).

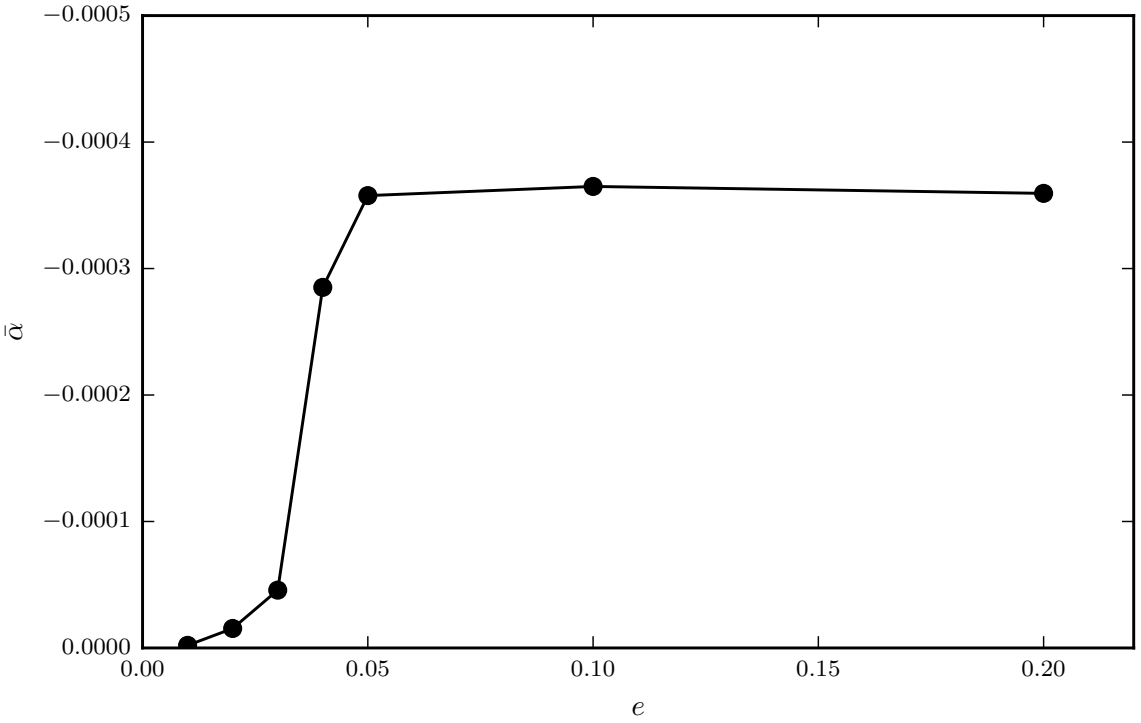

Fig. 4.9 The averaged α-viscosity at saturation is shown scaling with the disc eccentricity.

Reynolds shear stress begins to dominate over the correlated velocity term, producing the plateau in α. The reason for the increased influence of this term is still not clear, but it is also manifest as a slightly positive value in the linear growth phase for high eccentricity. Further investigation must be made to confirm that this is not an artefact of the numerical methods, as the limits of this implementation could be exceeded for large eccentricities.

A rough scaling for α may be found by rewriting the energy dissipation rate (4.6) as

$$\partial_t \tilde{E}_{k,\mathrm{loss}} \approx \frac{\alpha}{\Omega} \int_{\zeta_{\mathrm{crit}}}^{\infty} p k_0^2 \varepsilon \, \mathrm{d}\zeta, \tag{4.13}$$

and then equating with (4.6). As expected, this gives $\alpha \propto \overline{\sqrt{\varepsilon}}$. In the averaged sense, then $\alpha \propto \tilde{E}_k$ (with a negative proportionality constant to fit the scaling), suggesting that α should indeed continue to grow with eccentricity.

Most instabilities in discs extract energy from the background differential rotation (shear). This instability rather extracts energy from the background eccentric oscillations, and so does not immediately guarantee outward angular momentum transport. Axisymmetric instabilities are known to produce very little angular momentum transport, so that the turbulent and numerical viscosities are able to mix down the angular momentum gradient. Each fluid parcel conserves its initial angular momentum, $\ell \propto \sqrt{\lambda}$, and so as the turbulence rearranges the fluid it transports angular momentum inwards, producing $\alpha \lesssim 0$! In a similar 2D axisymmetric model of tidally distorted discs, Ryu and Goodman (1994) also found negligible angular momentum transport (albeit being quite dependent on the initial conditions). A small negative α is also produced, for example, in weak 3D convective instabilities, where the shear restricts the evolution to be effectively 2D axisymmetric (Lesur and Ogilvie, 2010). Therefore, present results are expected to be valid in 3D discs when the Keplerian shear dominates over the secondary instability, which could be expected for discs of moderate eccentricity. It is speculated then for a 3D local model with sufficiently large forcing (eccentricity), that the turbulence could overcome the tendency towards axisymmetry by the shear, and produce $\alpha > 0$. This would be of interest to investigate in future 3D eccentric shearing box simulations, and compare with the work of Papaloizou (2005a) who found an $\alpha \sim 10^{-3}$ for $e = 0.1$.

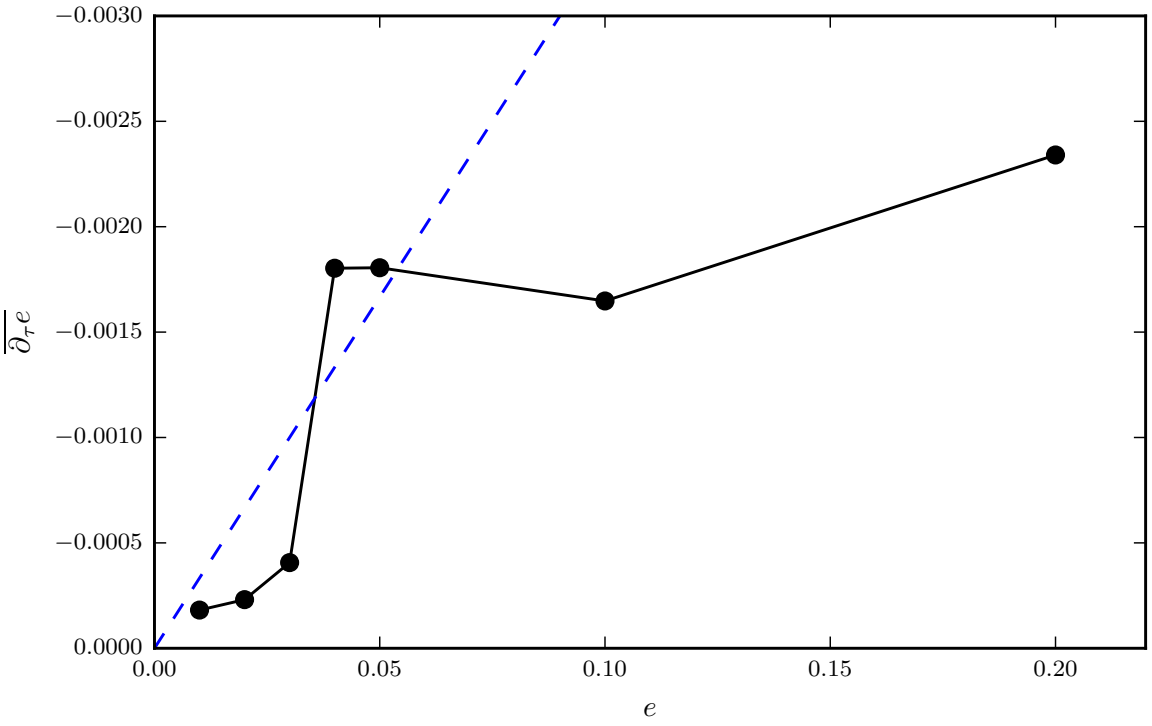

Fig. 4.10 The averaged eccentricity decay rate at saturation is shown scaling with the disc eccentricity. The eccentricity growth rate by the 3:1 eccentric Lindblad resonance found by Lubow (2010) is also given for reference (blue dotted line).

4.4 Eccentricity evolution

The integral (2.34) around the disc may also be computed discretely within the implemented code, assuming the radial structure of a stationary alpha-disc with constant $\alpha(r)$. The scaling of the eccentricity decay rate in this model is given in Figure 4.10, which suggests eccentricity decay times on the order of 50 to 100 orbital periods. It is a bit surprising that $\partial_\tau e$ plateaus; however, as this value is also dependent on the Reynolds stresses, the calculation becomes increasingly sensitive to numerical dissipation for high eccentricities. In reality, the nonlinear evolution of this instability is also likely to modify the global disc structure with increasing eccentricity.

Assuming a constant alpha-disc model, Lubow (2010) found an eccentricity growth rate driven by the eccentric Lindblad resonance of

$$\partial_\tau e \sim \frac{e}{10\mathcal{P}_b}, \tag{4.14}$$

where $\mathcal{P}_b$ is the binary orbit period relative to the local disc period. This growth rate is shown in Figure 4.10 for the 3:1 eccentric inner Lindblad resonance which is thought to be active in Superhump binaries. This energy absorption from the eccentric mode by the saturated parametric instability thus appears to be a promising means of balancing rapid eccentricity growth due to mean-motion resonances.

Chapter 5

Conclusions

The viability of implementing a well-balanced numerical method based on the local eccentric disc model has been demonstrated in this work, in addition to its effectiveness at studying local instabilities inherent to eccentric discs. Just as the linear theory for the inertial wave parametric instability produced significantly higher growth rates in a vertically stratified disc (Ogilvie and Barker, 2014; Papaloizou, 2005b), the nonlinear evolution and saturation has interesting differences as the vertical structure localises the effective region of the secondary instability. Below a critical height, the nonlinear effects are very weak; yet far above this critical height, the density is too low for the dissipation there to contribute significantly. There was some success at modelling this interplay using a vertical energy balance, shedding light on the observed scaling of the saturation energy with eccentricity in the strongly nonlinear regime.

This nonlinear regime of the axisymmetric instability was also found to be quite inefficient at transporting angular momentum. This result is expected to remain valid in 3D models for small eccentricity; however, more significant (outward) angular momentum transport could be expected for large eccentricities when the azimuthal symmetry is broken as the turbulence overcomes the Keplerian shear. Studying this impact of the nonaxisymmetry on the α-viscosity at large eccentricity would require development of a 3D numerical model for the eccentric local model, but may help explain the occurrence of superoutbursts in SU UMa stars. Further investigation into the impacts of an eccentricity gradient and disc twist on this nonlinear evolution would also be of interest, as well as the implications of using less-compressive (non-isothermal) thermodynamics. Nonetheless, the saturation of this parametric instability appears to be a promising dissipation mechanism for balancing the exponential growth of eccentricity due to mean-motion resonances. The stresses produced in the steady

turbulent state were found to effectively damp the eccentricity, giving estimated decay times of 50 to 100 orbital periods.

These presented results are applicable to any continually perturbed eccentric disc of small eccentricity, where the balance with the eccentricity decay studied here might set a stable disc eccentricity. In particular, in protoplanetary discs where embedded planets may continually perturb the disc, this eccentricity decay mechanism may have further-reaching effects on the evolution and damping of planet eccentricity (Bitsch et al., 2013; Goldreich and Sari, 2003; Papaloizou et al., 2001). Finally, in Cataclysmic binary systems, the eccentricity damping rate found here is comparable to the estimated growth by the 3:1 Lindblad resonance.

References

Armitage, P. J. (2011). Dynamics of Protoplanetary Disks. *Annual Review of Astronomy and Astrophysics*, 49(1):195–236.

Balbus, S. A. and Hawley, J. F. (1991). A powerful local shear instability in weakly magnetized disks. I - Linear analysis. *The Astrophysical Journal*, 376:214.

Barker, A. J. and Ogilvie, G. I. (2014). Hydrodynamic instability in eccentric astrophysical discs. *Monthly Notices of the Royal Astronomical Society*, 445(1):2637–2654.

Bitsch, B., Crida, A., Libert, A. S., and Lega, E. (2013). Highly inclined and eccentric massive planets. I. Planet-disc interactions. *Astronomy and Astrophysics*, 555:A124.

Botta, N., Klein, R. I., Langenberg, S., and Lützenkirchen, S. (2004). Well balanced finite volume methods for nearly hydrostatic flows. *Journal of Computational Physics*, 196(2):539–565.

Chandrashekar, P. and Klingenberg, C. (2015). A second order well-balanced finite volume scheme for Euler equations with gravity. *SIAM Journal on Scientific Computing*, 37(3):B382–B402.

Godunov, S. K. (1959). A difference method for numerical calculation of discontinuous solutions of the equations of hydrodynamics. *Matematicheskii Sbornik*.

Goldreich, P. and Lynden-Bell, D. (1965). I. Gravitational stability of uniformly rotating disks. *Monthly Notices of the Royal Astronomical Society*, 130(2):97–124.

Goldreich, P. and Sari, R. (2003). Eccentricity evolution for planets in gaseous disks. *The Astrophysical Journal*, 585(2):1024–1037.

Goldreich, P. and Tremaine, S. (1981). The origin of the eccentricities of the rings of Uranus. *Astrophysical Journal*, 243:1062–1075.

Gottlieb, S., Shu, C.-W., and Tadmor, E. (2001). Strong Stability-Preserving High-Order Time Discretization Methods. *SIAM Review A*, 43(1):89–112.

Greenberg, J. M. and Leroux, A. Y. (1996). A well-balanced scheme for the numerical processing of source terms in hyperbolic equations. *SIAM Journal on Numerical Analysis*, 33(1):1–16.

Käppeli, R. and Mishra, S. (2016). A well-balanced finite volume scheme for the Euler equations with gravitation. *Astronomy and Astrophysics*, 587:A94.

King, A. R., Pringle, J. E., and Livio, M. (2007). Accretion disc viscosity: how big is alpha? *Monthly Notices of the Royal Astronomical Society*, 376(4):1740–1746.

Kley, W. and Dirksen, G. (2006). Disk eccentricity and embedded planets. *Astronomy and Astrophysics*, 447(1):369–377.

Kley, W., Papaloizou, J. C. B., and Ogilvie, G. I. (2008). Simulations of eccentric disks in close binary systems. *Astronomy and Astrophysics*, 487(2):671–687.

Lesur, G. and Ogilvie, G. I. (2010). On the angular momentum transport due to vertical convection in accretion discs. *Monthly Notices of the Royal Astronomical Society: Letters*, 404(1):L64–L68.

LeVeque, R. J. (1997). Wave propagation algorithms for multidimensional hyperbolic systems. *Journal of Computational Physics*, 131(2):327–353.

Lin, D. N. C. and Pringle, J. E. (1976). Numerical Simulation of Mass Transfer and Accretion Disc Flow in Binary Systems. In *Structure and Evolution of Close Binary Systems*, pages 237–252. Springer Netherlands, Dordrecht.

Lubow, S. H. (1991). A model for tidally driven eccentric instabilities in fluid disks. *The Astrophysical Journal*, 381:259–267.

Lubow, S. H. (2010). Eccentricity growth rates of tidally distorted discs. *Monthly Notices of the Royal Astronomical Society*, 406(1):2777–2786.

Lyubarskij, Y. E., Postnov, K. A., and Prokhorov, M. E. (1994). Eccentric accretion discs. *Monthly Notices of the Royal Astronomical Society*, 266(3):583–596.

Marzari, F., Scholl, H., Thebault, P., and Baruteau, C. (2009). On the eccentricity of self-gravitating circumstellar disks in eccentric binary systems. *Astronomy and Astrophysics Supplement Series*, 508(3):1493–1502.

Murray, J. R. (1996). SPH simulations of tidally unstable accretion disks in cataclysmic variables. *Monthly Notices of the Royal Astronomical Society*, 279(2):402–414.

Ogilvie, G. I. (2001). Non-linear fluid dynamics of eccentric discs. *Monthly Notices of the Royal Astronomical Society*, 325(1):231–248.

Ogilvie, G. I. and Barker, A. J. (2014). Local and global dynamics of eccentric astrophysical discs. *Monthly Notices of the Royal Astronomical Society*, 445(1):2621–2636.

Ogilvie, G. I. and Latter, H. N. (2013). Hydrodynamic instability in warped astrophysical discs. *Monthly Notices of the Royal Astronomical Society: Letters*, 433(3):2420–2435.

Okazaki, A. T., Kato, S., and Fukue, J. (1987). Global trapped oscillations of relativistic accretion disks. *Astronomical Society of Japan*, 39:457–473.

Papaloizou, J. C. B. (2005a). Global numerical simulations of differentially rotating disks with free eccentricity. *Astronomy and Astrophysics*, 432(3):757–769.

Papaloizou, J. C. B. (2005b). The local instability of steady astrophysical flows with non circular streamlines with application to differentially rotating disks with free eccentricity. *Astronomy and Astrophysics*, 432(3):743–755.

Papaloizou, J. C. B. and Lin, D. N. C. (1995). Theory Of Accretion Disks I: Angular Momentum Transport Processes. *Annual Review of Astronomy and Astrophysics*, 33(1):505–540.

Papaloizou, J. C. B., Nelson, R. P., and Masset, F. (2001). Orbital eccentricity growth through disc-companion tidal interaction. *Astronomy and Astrophysics*, 366(1):263–275.

Pringle, J. E. (1981). Accretion Discs in Astrophysics. *Annual Review of Astronomy and Astrophysics*, 19(1):137–160.

Regev, O. and Umurhan, O. M. (2008). On the viability of the shearing box approximation for numerical studies of MHD turbulence in accretion disks. *Astronomy and Astrophysics*, 481(1):21–32.

Ryu, D. and Goodman, J. (1994). Nonlinear evolution of tidally distorted accretion disks: Two-dimensional simulations. *The Astrophysical Journal*, 422:269–288.

Shakura, N. I. and Sunyaev, R. A. (1973). Black holes in binary systems. Observational appearance. *Astronomy and Astrophysics*, 24:337–355.

Slyz, A. and Prendergast, K. H. (1999). Time-independent gravitational fields in the BGK scheme for hydrodynamics. *Astronomy and Astrophysics Supplement Series*, 139(1):199–217.

Spitzer, L. (1962). *Physics of fully ionized gases*. Interscience, New York, NY, 2 edition.

Sweby, P. K. (1984). High Resolution Schemes Using Flux Limiters for Hyperbolic Conservation Laws. *SIAM Journal on Numerical Analysis*, 21(5):995–1011.

Syer, D. and Clarke, C. J. (1992). The viscous evolution of elliptical accretion discs. *Monthly Notices of the Royal Astronomical Society*, 255(1):92–104.

Toomre, A. (1964). On the gravitational stability of a disk of stars. *The Astrophysical Journal*, 139:1217.

Toro, E. F. (1999). *Riemann Solvers and Numerical Methods for Fluid Dynamics*. Springer, Berlin, Heidelberg, 2 edition.

Whitehurst, R. (1988). Numerical simulations of accretion discs – I. Superhumps: a tidal phenomenon of accretion discs. *Monthly Notices of the Royal Astronomical Society*, 232(1):35–51.

Wienkers, A. F. (2016). Part I: On the shearing box approximation for the compressible Euler equations.

Appendix A

Relevant geometric quantities

The relevant geometric quantities describing the orbital coordinates with oscillating height are given (primed, or in ζ), alongside the original or unchanged quantities reproduced from Ogilvie and Barker (2014) for convenience.

$$g_{\lambda\lambda} = R_\lambda^2 \tag{A.1}$$

$$g^{\lambda\lambda} = \frac{R^2 + R_\phi^2}{R^2 R_\lambda^2} \tag{A.2}$$

$$g_{\lambda\phi} = g_{\phi\lambda} = R_\lambda R_\phi \tag{A.3}$$

$$g^{\lambda\phi} = g^{\phi\lambda} = -\frac{R_\phi}{R^2 R_\lambda} \tag{A.4}$$

$$g_{\phi\phi} = R^2 + R_\phi^2 \tag{A.5}$$

$$g^{\phi\phi} = \frac{1}{R^2} \tag{A.6}$$

$$g_{\zeta\zeta} = \frac{1}{g^{\zeta\zeta}} = H^2 \tag{A.7}$$

$$J'(\lambda,\phi,\zeta) = HJ(\lambda,\phi,z) = \frac{H\lambda\left(1+(e-\lambda e')\cos\theta - \lambda e\omega'\sin\theta\right)}{\left(1+e\cos\theta\right)^3} \tag{A.8}$$

$$\Gamma^{\lambda}_{\lambda\phi} = \Gamma^{\lambda}_{\phi\lambda} = \frac{R_{\lambda\phi}}{R_\lambda} - \frac{R_\phi}{R} \tag{A.9}$$

$$\Gamma^{\lambda}_{\phi\phi} = -\frac{R^2 + 2R_\phi^2 - RR_{\phi\phi}}{RR_\lambda} \tag{A.10}$$

$$\Gamma^{\phi}_{\phi\phi} = \frac{2R_\phi}{R} \tag{A.11}$$

$$\Gamma^{\phi}_{\lambda\phi} = \Gamma^{\phi}_{\phi\lambda} = \frac{R_\lambda}{R} \tag{A.12}$$

$$\Delta' = \Delta + \frac{\dot{H}}{H} = \sqrt{\frac{GM}{\lambda^3}}\frac{\lambda(1+e\cos\theta)\left(e'\sin\theta - e\omega'(\cos\theta+e)\right)}{1+(e-\lambda e')\cos\theta - \lambda e\omega'\sin\theta} + \frac{\dot{H}}{H} \tag{A.13}$$

$$\Phi_2 = \frac{GM}{\lambda^3}\left(1+e\cos\theta\right)^3 \tag{A.14}$$

$$\Omega_i = \partial_i\Omega \tag{A.15}$$

$$R_i = \partial_i R \tag{A.16}$$

Appendix B

Code validation

A test suite of five 1D tests designed by Toro (1999) define macroscopic Riemann problems producing varying magnitudes and combinations of shocks, rarefactions, and contact discontinuities. These are summarised in Table B.1, including the simulation time and the location, x_c, of the initial discontinuity. A thorough description of each test, in addition to the performance of the WAF and MUSCL-Hancock schemes using different limiters is investigated in Wienkers (2016).

Test	Description	t_{stop}	x_c	ρ_L	u_L	p_L	ρ_R	u_R	p_R
1	Modified Sod	0.2	0.3	1.0	0.75	1.0	0.125	0.0	0.1
2	123 Problem	0.12	0.5	1.0	-2.0	0.4	1.0	2.0	0.4
3	Blast Wave	0.012	0.5	1.0	0.0	1000.0	1.0	0.0	0.01
4	Shock Collision	0.035	0.4	6.0	19.5975	460.894	6.0	-6.19633	46.095
5	Stationary Contact	0.012	0.8	1.0	-19.5975	1000.0	1.0	-19.5975	0.01

Table B.1 Summary of the 1D test regimen.

The finite volume implementation described in §3.1 using TVD RK2SSP integration with the Minbee limiter and exact Riemann solver (shown with blue ○'s) is compared against the often-used MUSCL-Hancock TVD integration scheme with the Minbee limiter and HLLC approximate Riemann solver (shown with red ×'s). The results of each of these tests are given on the following pages.

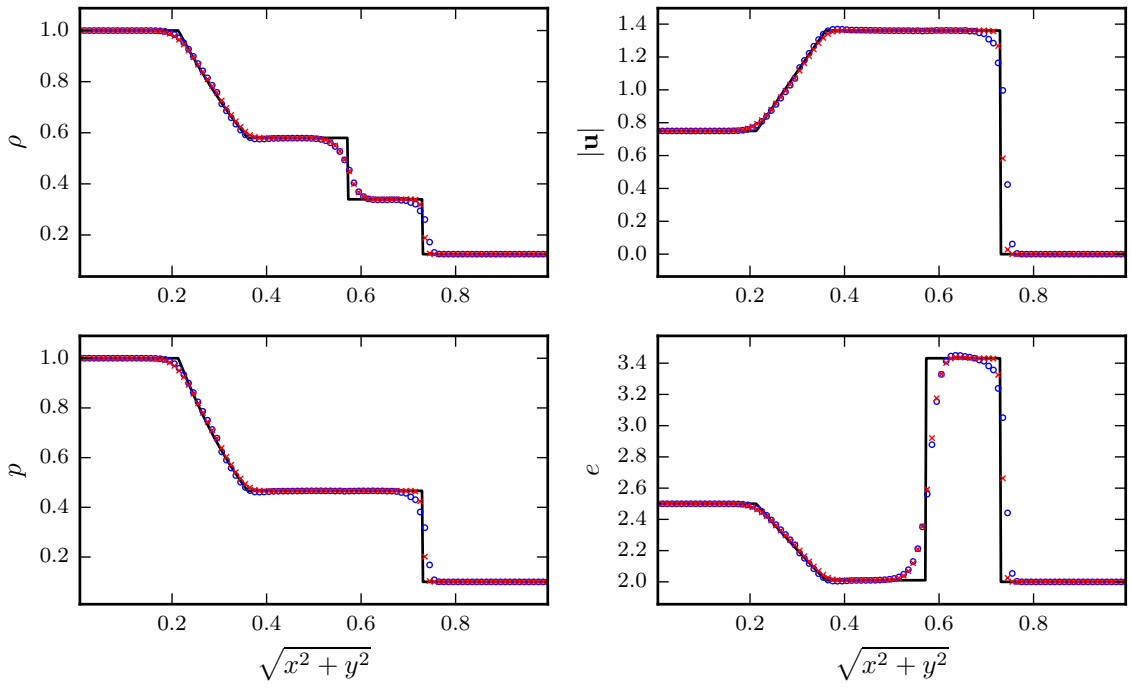

Fig. B.1 Test 1 at $t = 0.2$, with the exact Riemann solution for reference.

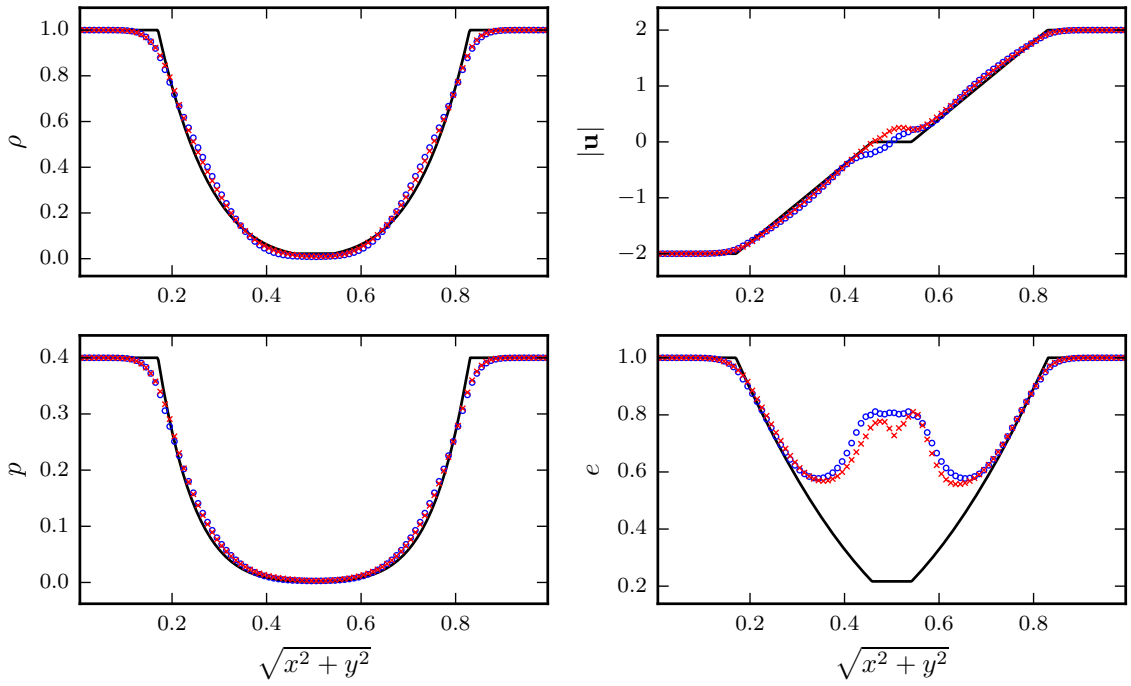

Fig. B.2 Test 2 at $t = 0.12$, with the exact Riemann solution for reference.

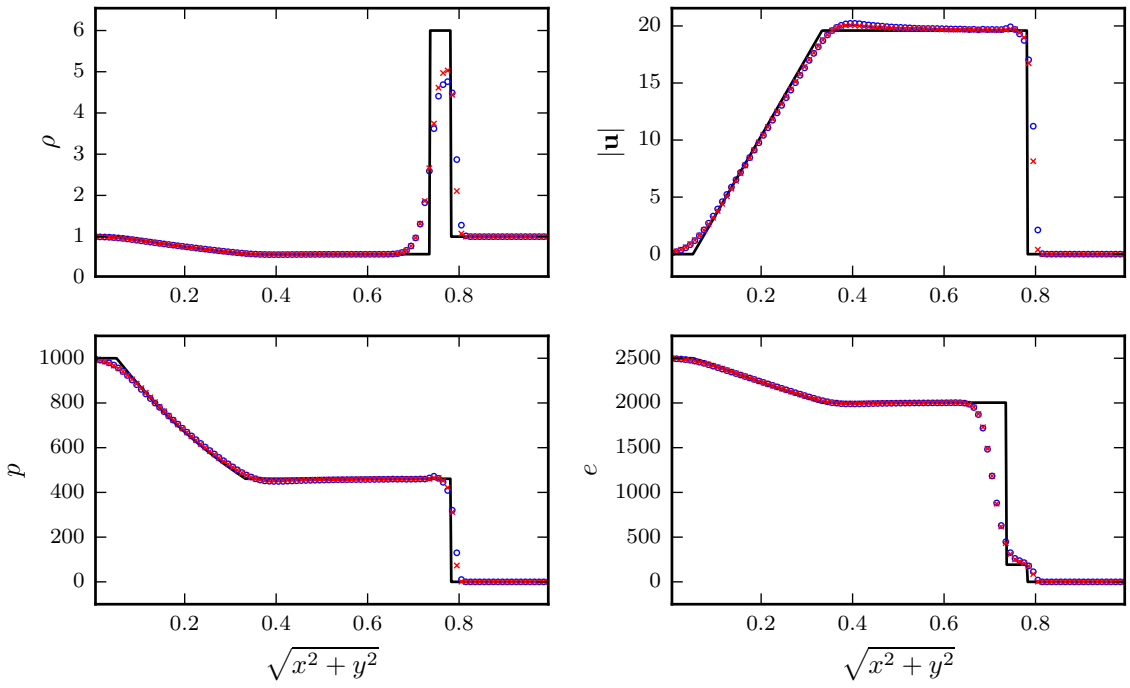

Fig. B.3 Test 3 at $t = 0.012$, with the exact Riemann solution for reference.

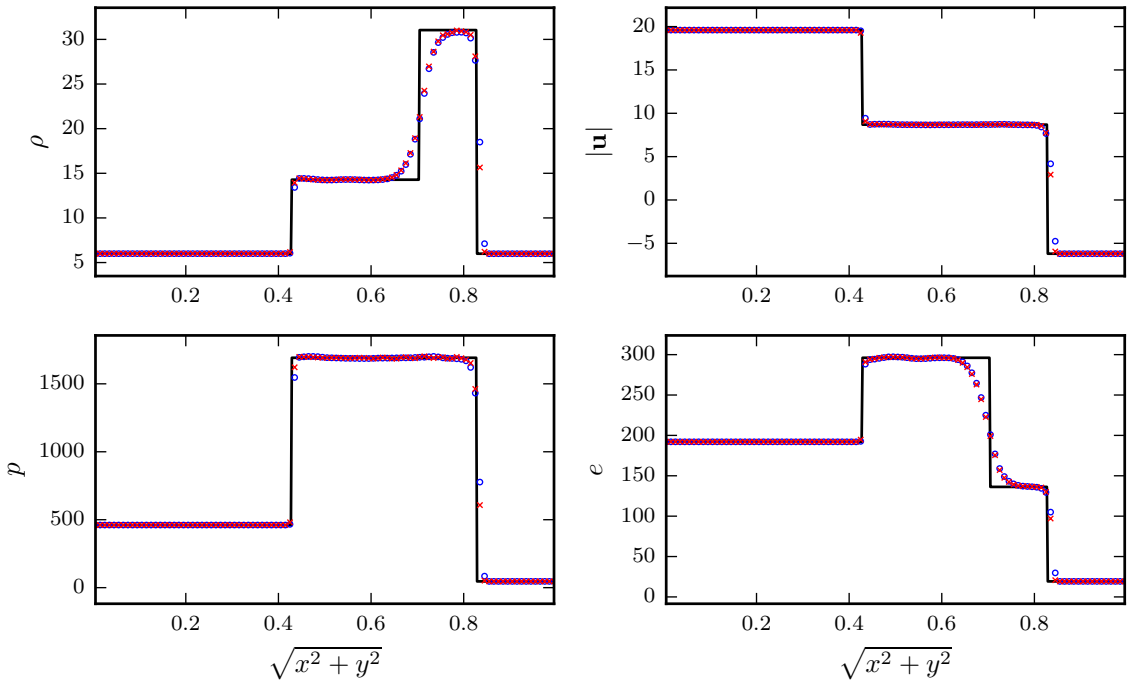

Fig. B.4 Test 4 at $t = 0.035$, with the exact Riemann solution for reference.

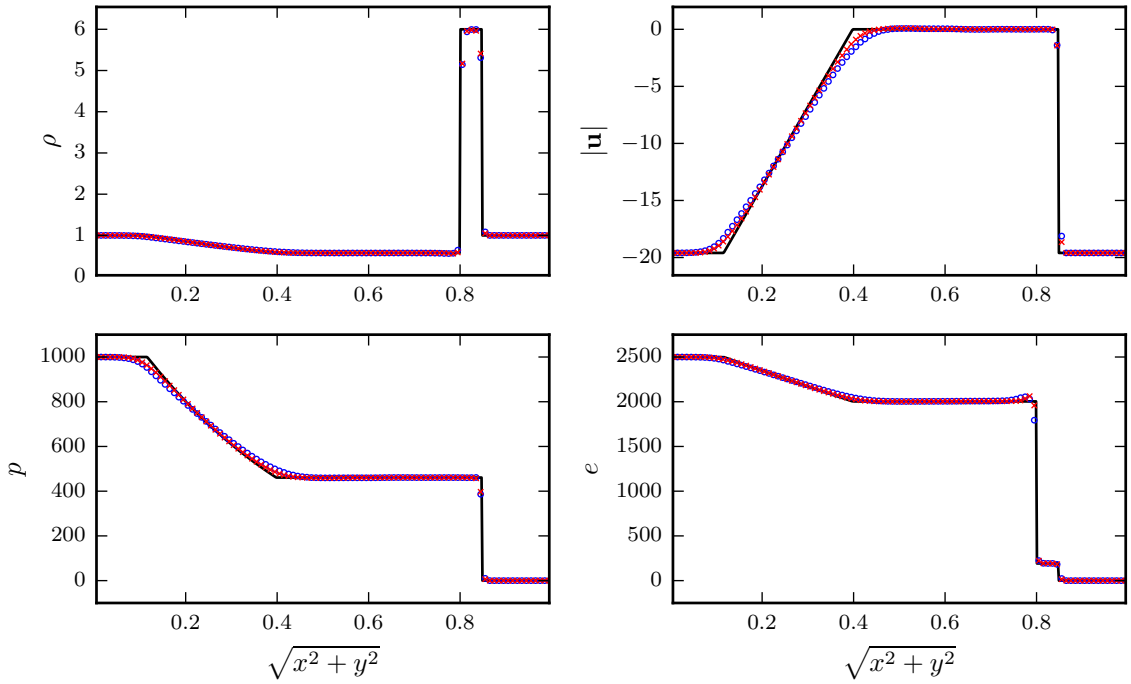

Fig. B.5 Test 5 at $t = 0.012$, with the exact Riemann solution for reference.